Carbon Enrichment in the Lithospheric Mantle: Evidence from the Melt Inclusions in Mantle Xenoliths from the Hainan Basalts

XU Xin, TIAN Wei, ZHANG Lifei* and LI Huijuan

The Key Laboratory of Orogenic Belts and Crustal Evolution, Ministry of Education, School of Earth and Space Sciences, Peking University, Beijing 100871, China

Abstract: It is generally believed that the lithospheric mantle and the mantle transition zone are important carbon reservoirs. However, the location of carbon storage in Earth's interior and the reasons for carbon enrichment remain unclear. In this study, we report CO_2-rich olivine-hosted melt inclusions in the mantle xenoliths of late Cenozoic basalts from the Penglai area, Hainan Province, which may shed some light on the carbon enrichment process in the lithospheric mantle. We also present a detailed petrological and geochemical investigation of the late Cenozoic basalts and mantle xenoliths from northern Hainan Island. The collected samples of late Cenozoic Hainan Island basalts belong to both alkaline and subalkaline series, showing fractionated REE patterns with high $(La/Yb)_N$ values of 3.52–11.77, which are typical for OIB. Based on Al-in-olivine thermometry, the temperatures estimated for the mantle xenoliths can be divided into two groups. One group has temperatures of less than 1050°C, and the other group has temperature ranging from 1050°C to 1282°C. Clinopyroxene $(La/Yb)_N$–Ti/Eu and clinopyroxene Ca/Al–$Mg^{\#}$ diagrams indicate that the mantle peridotite experienced metasomatism from both silicate and carbonate melts. Melt inclusions in the olivine of mantle xenoliths include (1) CO_2 bubble–rich melt inclusions; (2) multiphase melt inclusions (glass + CO_2 bubble + daughter minerals); (3) pure glass melt inclusions. Magnesite is a daughter mineral in the olivine-hosted melt inclusions, which could be interpreted as a secondary mineral formed by the interactions of CO_2-rich fluids with an olivine host, due to post-entrapment effects. The glasses in olivine-hosted melt inclusions have high SiO_2 contents (60.21–77.72 wt%). Our results suggest that a considerable amount of CO_2-rich melt inclusions are captured in the lithospheric mantle during metasomatism. The lithospheric mantle can therefore act as is a ‘carbon trap’, with much CO_2 being absorbed by the lithospheric mantle in this way.

Key words: melt inclusions, lithospheric mantle, metasomatism, carbon trap, Hainan Island

Citation: Xu et al., 2023. Carbon Enrichment in the Lithospheric Mantle: Evidence from the Melt Inclusions in Mantle Xenoliths from the Hainan Basalts. Acta Geologica Sinica (English Edition), 97(1): 358–375. DOI: 10.1111/1755-6724.15043

1 Introduction

Earth’s mantle is the largest carbon reservoir, containing approximately five orders of magnitude more carbon than the atmosphere-ocean system (Sleep and Zahnle, 2001; Coltice et al., 2004). It is generally believed that the lithospheric mantle and the mantle transition zone are important carbon reservoirs. However, the location of carbon storage in Earth's interior and the mechanisms for carbon enrichment are unclear. The budget of CO_2 in Earth's atmosphere plays a pivotal role in maintaining a habitable climate throughout geological history (Dasgupta and Hirschmann, 2010). It is widely known that carbon degassed from the deep mantle to the surface during volcanism. The extent and efficiency of CO_2 degassing is dependent on the depth and the degree of magma generation. If melting initiates at shallow depths in the mantle, carbon outgassing will be poor and vice versa (Dasgupta and Hirschmann, 2010). Thus, quantifying the content of CO_2 in the volcanic system is important for understanding deep carbon recycling (Moore and Bodnar, 2019).

As the magma rises from deep mantle to Earth's surface, dissolved volatiles (pure CO_2 and H_2O) in the magma are lost, due to the decrease in pressure. It is therefore not reliable to investigate the degassing history of a volcanic system by directly using volatile abundances in bulk rocks or tephras (Dixon et al., 1995; Wallace et al., 2015; Moore et al., 2015; Wieser et al., 2020; Tang et al., 2022). As an alternative, melt inclusions (MI) are now extensively studied in a wide range of volcanic and intrusive igneous rocks, for the investigation of volatiles in magmas and mantle sources. Melt inclusions are small droplets of silicate melt trapped in a growing crystal defect before eruption, representing the pre-eruptive/undegassed magmas at depth. Therefore, they are always used to estimate the CO_2 budget of pre-eruptive magmas (Roedder, 1979; Anderson et al., 2000; Hauri et al., 2002; Lowenstern, 2003; Wallace, 2005; Bodnar and Student, 2006; Esposito et al., 2011; Gazel et al., 2012; Wallace et al., 2015; Moore et al., 2015; Aster et al., 2016; Moore and Bodnar, 2019). We should caution that volatiles in melt inclusions have been influenced by post-entrapment crystallization effects, diffusive ‘Fe and H^+ loss’ through

* Corresponding author. E-mail: lfzhang@pku.edu.cn

host crystals and shrink bubble formation during cooling (Frezzotti, 2001; Danyushevsky et al., 2002; Kent, 2008; Bucholz et al., 2013; Moore et al., 2015; Wallace et al., 2015). However, if the post-entrapment crystallization effects are corrected for, the melt inclusions provide reliable information regarding volatile composition.

In recent years, studies have mainly focused on reconstruction of the budget of CO_2 in the MIs trapped in olivine phenocrysts, using a variety of methods, such as (1) measurement of bubble CO_2 density by Raman spectroscopy (e.g., Esposito et al., 2011; Hartley et al., 2014; Moore et al., 2015; Aster et al., 2016), (2) equation of state calculations (Shaw et al., 2008, 2010; Wanless et al., 2014, 2015; Moore et al., 2015; Hauri et al., 2017; Tucker et al., 2019), (3) heating the melt inclusions to homogenize and dissolve shrinkage bubbles back into the melt (e.g., Hauri, 2002; Mironov et al., 2015; Wallace et al., 2015; Tuohy et al., 2016).

Olivine-hosted melt inclusions in mantle xenoliths or xenocrysts have received less research attention. As silicate melts transport the deep carbon to the surface, melt inclusions trapped in mantle peridotite can record the compositions of melt at mantle depth and provide a unique window for understanding the degassing process (Frezzotti et al., 2012). The upwelling magmas ascend through the lithospheric mantle by interacting with the upper mantle, resulting in the alteration of physico–chemical properties. At the same time, significant quantities of CO_2 are lost from the melt and entrapped by the upper mantle. This study attempts to answer the following question: how does the lithospheric mantle ‘capture carbon’?

In this work, we studied the olivine-hosted melt inclusions in the mantle xenoliths of late Cenozoic basalts from the Penglai area, Hainan Province, with detailed petrographic observation, electron microprobe analysis (EMPA) for composition and laser Raman microprobe analysis for CO_2 characterization. We also present a detailed petrological and geochemical investigation of the late Cenozoic basalts from northern Hainan Island. This study provides important evidence showing that the lithospheric mantle is a ‘carbon trap’. These results also provide insights into the metasomatic interaction between the melt and the lithospheric mantle, as well as the deep magmatic processes.

2 Geological Background and Samples

2.1 Geological background

Hainan Island, situated at the convergent boundary of the Eurasian, Indo-Australian and Pacific plates, is separated from the Cathaysia Block of the South China Block (SCB) by the Qiongzhou Strait (Fig. 1a). late Cenozoic basalts are distributed in north Hainan Island, with a coverage of approximately 4000 km^2, representing the largest Cenozoic basalt area in southeastern China (Fig. 1b; Metcalfe et al., 1993; Huang et al., 1993; Xu et al., 2020; Wei et al., 2021; Zhao et al., 2021). About 100 volcanoes have been discovered in the north of Hainan Island. They are characterized by fissure eruptions and central eruptions, forming a lot of lava cones. The volcanism began in the late Oligocene (23.3 Ma) and ceased in the Holocene (<0.012 Ma), the eruption being particularly strong in the Pleistocene and Holocene (Flower et al., 1992; Ho et al., 2000; Fan et al., 2004). Previous studies divided Hainan Island Cenozoic basalts into five eruptive episodes, according to K-Ar and Ar-Ar dating: Penglai Formation in the Miocene–Pliocene, Duowenling Formation in the early Pleistocene, Dongying Formation in the middle Pleistocene, Daotang Formation in the late Pleistocene and Leihuling Formation in the Holocene (Fig. 2; Sun, 2003). Hainan Island late Cenozoic basalts are mainly composed of tholeiites, with a small proportion of alkali basalts. These basalts are characterized by porphyritic and vesicular structures. The main phenocrysts are plagioclase, olivine and pyroxene. The matrix consists of plagioclase, pyroxene and volcanic glass. In addition to basalts, there are also a small number of pyroclastic rocks, mainly tuff, volcanic breccia and volcanic agglomerate, which are distributed around the Leihuling area of northern Hainan Island. In addition, mantle xenoliths can be found in the alkali basalts in the Penglai area (Fig. 2), suggesting that magma ascent was rapid (Xu et al., 2002). Alkali basalts also contain xenocrysts formed after the disintegration of xenoliths. The size of the mantle xenoliths is approximately 1–3 cm in diameter and mantle xenoliths are mainly spinel lherzolite, consisting of olivine, clinopyroxene and orthopyroxene.

Based on the initial opening time of the South China Sea (>32–16 Ma), many researchers proposed that the spreading time of the South China Sea is prior to the eruption time of the Hainan Island Cenozoic basalts. The extension resulted in a great number of depressions, uplifts and right-lateral strike-slip faults from the South China Sea to the Chinese mainland (Chung et al., 1997; Lei et al., 2009; Sun et al., 2009), the major faults being divisible into two types: E–W faults and NE–SW faults, which controlled the volcanic activities and distribution of the stratification, respectively. The E–W oriented faults dominated by the Paleo-Tethyan tectonic regime are composed mainly of (from north to south) the Wangwu–Wenjiao, Jianfeng–Diaoluo and Jiusuo–Lingshui faults, which are closely connected to the distribution of depressions, uplifts and volcanic rocks in the area. The NE–SW oriented faults dominated by the Pacific tectonic regime consist primarily of the Baisha and Chenxi–Bangxing faults.

In recent years, a young plume named the ‘Hainan plume’ was observed through geophysical studies. The Hainan plume is characterized by a low-velocity structure, lying close to the subduction zones and far away from superplumes (Lebedev and Nolet, 2003; Montelli et al., 2006; Lei et al., 2009; Xia et al., 2016; Li, 2021; Lu et al., 2022; Wang et al., 2022). Zhao (2007) and Zhao et al. (2021) further proposed that low-V_p anomalies prevail across the whole mantle beneath the Southeastern Asian basalt province (SABP), where the Hainan plume is the strongest one and one of twelve hypothesized plumes that originated from the lower mantle around the world. These features make the Hainan plume provocative and special, because it provides insight into a rare example of a young

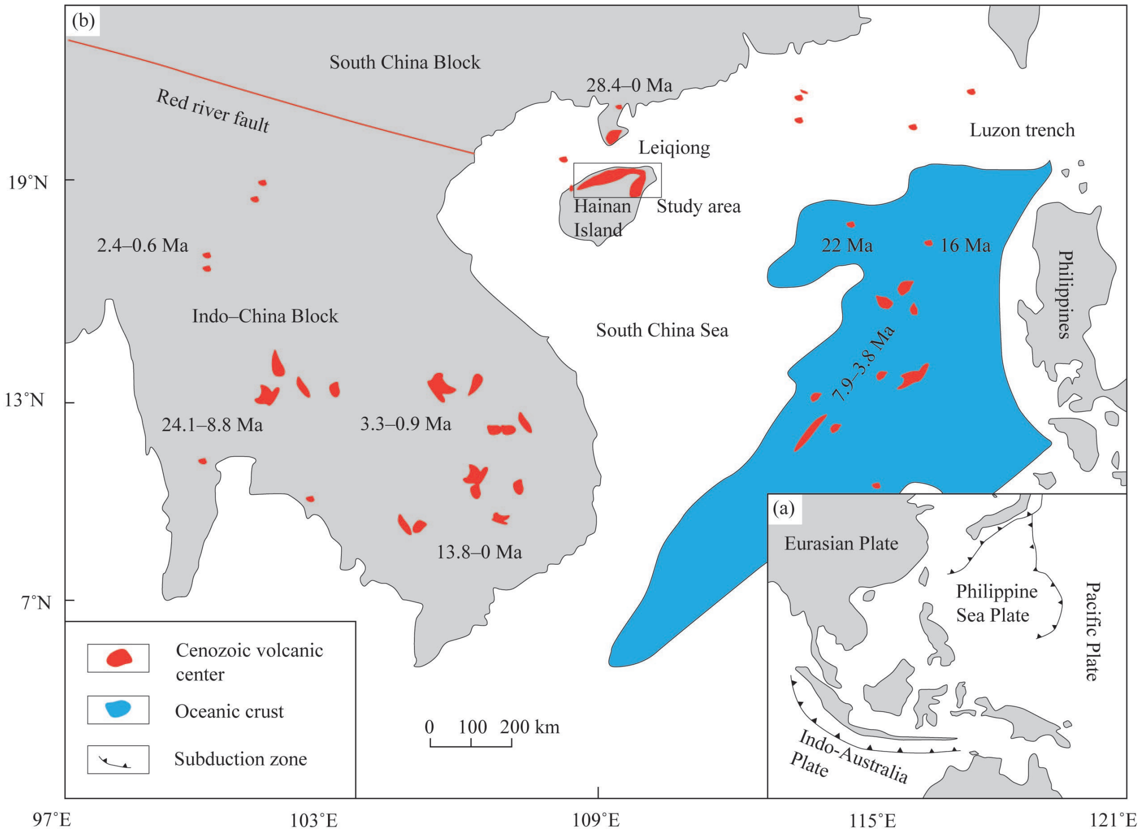

Fig. 1. (a) Small sketch map showing the tectonic situation of the South China Sea. This area is located at the triple junction of the Eurasian, Indo-Australian and Pacific (Philippine) plates, surrounded by multiple subduction zones; (b) sketch map of the South China Sea region, showing the late Cenozoic volcanic centers, with ages. The map is modified from Yan et al. (2018). The Leiqiong area refers to the Leizhou Peninsula and the northern part of Hainan Island. The ages and areas of individual basalts are from Hoang et al. (1996), Ho et al. (2000) and Yan et al. (2018).

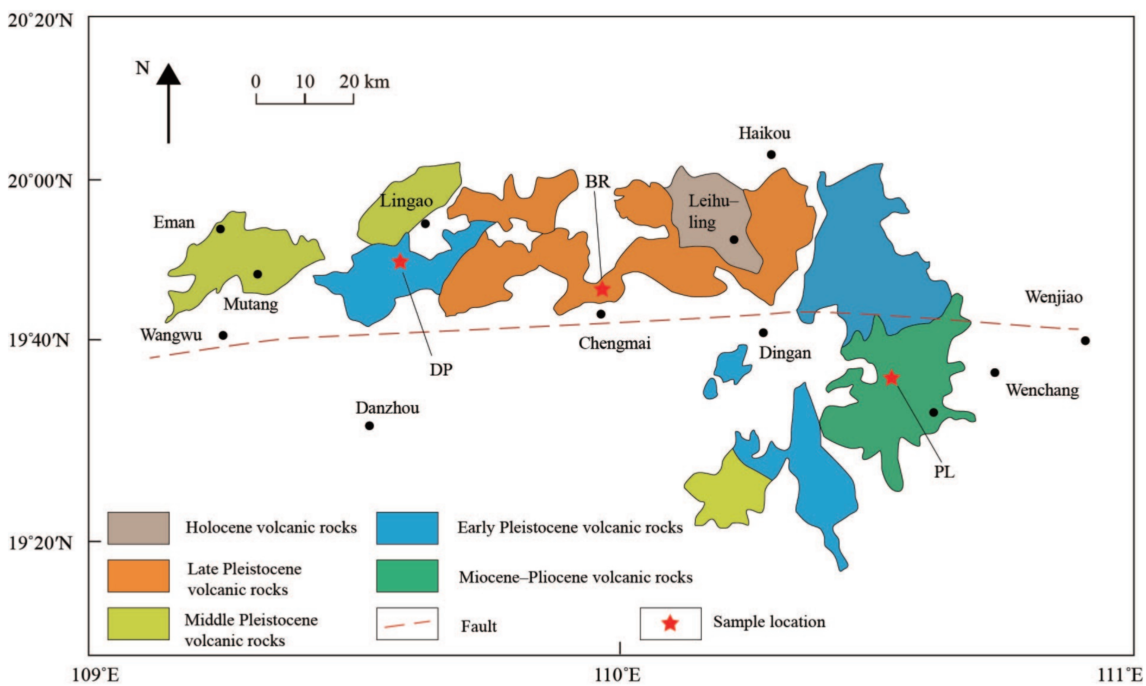

Fig. 2. Distribution and sample locations of late Cenozoic basalts on Hainan Island (modified from Sun, 2003). Basalts are subdivided into five eruptive episodes, according to their age data (Sun, 2003).

mantle plume near deep subduction zones, rather than a lower mantle superplume (Wang et al., 2013).

2.2 Petrology of basalt samples and mantle xenoliths

A total of 58 samples were collected from northern Hainan Island (Fig. 4a–d), including 50 samples from the Penglai area (PL), 3 samples from Duowenling (DP; Figs. 2, 4c) and 5 samples from Chengmai (BR; Figs. 2, 4d). 30 out of the 50 from the Penglai area were selected for detailed melt inclusion studies, as 30 of the basalt samples contained mantle xenoliths (Figs. 2–3, 4a, b). These samples were mainly from the same eruption as the 'Penglai Formation' and formed in the Miocene–Pliocene (5–3 Ma). Late Cenozoic basalts from the Penglai area are grey-black in color, composed of approximately 35% phenocrysts. The phenocrysts consist of plagioclase (15%), olivine (5%), clinopyroxene (Cpx, 5%), orthopyroxene (Opx, 3%–5%) and are euhedral to subhedral, ranging from 0.5 to 2 mm in size. The matrix mainly consists of microlites of olivine, plagioclase and pyroxene (Fig. 4e). In addition, magnetite and glass are present in the groundmass (Fig. 4f, g). Olivine xenocrysts have clear compositional zoning (see the analytical results). On the back-scattered electron image, the central part is dark (rich in Mg), the rim is light (rich in Fe) and the width between the centre and the edge varies between olivine grains. According to field observations, a few of the fresh mantle peridotite xenoliths (spinel lherzolite) were found in the basalts (Fig. 4b). The xenoliths are yellow-green in color and 1–3 cm in size (Fig. 4b). The xenoliths consist of 65% olivine, 15% orthopyroxene, 18% clinopyroxene and 2% Cr-spinel. The olivine displays kink banding (Fig. 4h) and has a coarse granular texture with 120° dihedral angles between grain boundaries (Fig. 4h). The Cr-spinel is brownish to reddish -brown in plane-polarized light and occurs interstitially between olivine and pyroxene.

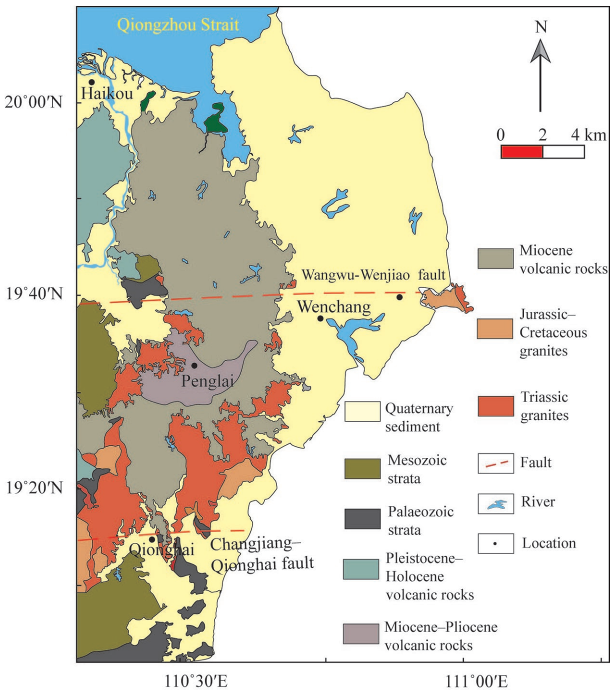

Fig. 3. Geological map of the Penglai volcanic-plutonic, Hainan Island, SE China (modified from BGGP, 1964).

2.3 Petrography of melt inclusions

Numerous olivine-hosted melt inclusions are distributed throughout the mantle xenoliths. According to the phases present at room temperature, olivine-hosted melt inclusions can be divided into three types, type I: CO_2 bubble-rich melt inclusions (Fig. 5a–d); Type II: multiphase melt inclusions (Fig. 5e–g); Type III: glass melt inclusions (Fig. 5h–i). Type I melt inclusions consist of a glass phase plus one bubble and are rounded, ellipsoidal to spherical and neck-down in shape. Type II melt inclusions are composed of multiple phases (glass + CO_2 bubble + daughter minerals) and are rectangle, elongate, neck-down and irregular in shape. Type III melt inclusions consist of pure glass and are both elongate and irregular in shape. Type II melt inclusions contain well-

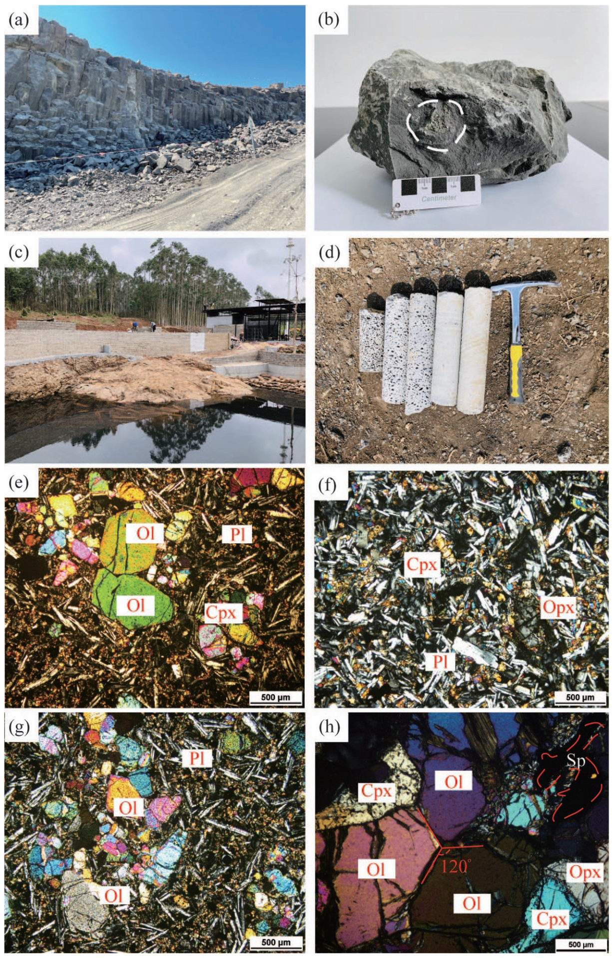

Fig. 4. Field photographs and photomicrographs of late Cenozoic basalts in the Penglai area, northern Hainan Island.

(a) 'Penglai Formation' basalt outcrop; (b) hand-specimen with xenolith; (c) 'Duowenling Formation' basalt outcrop; (d) 'Dongying Formation' basalt outcrop; (e) photomicrograph of late Cenozoic basalts in the Penglai area; (f) photomicrograph of late Cenozoic basalts in the Duowenling area; (g) photomicrograph of late Cenozoic basalts in the Chengmai area; (h) photomicrograph of xenoliths in the Penglai area. Ol–olivine; Cpx–clinopyroxene; Opx–orthopyroxene; Sp–spinel; Pl–plagioclase.

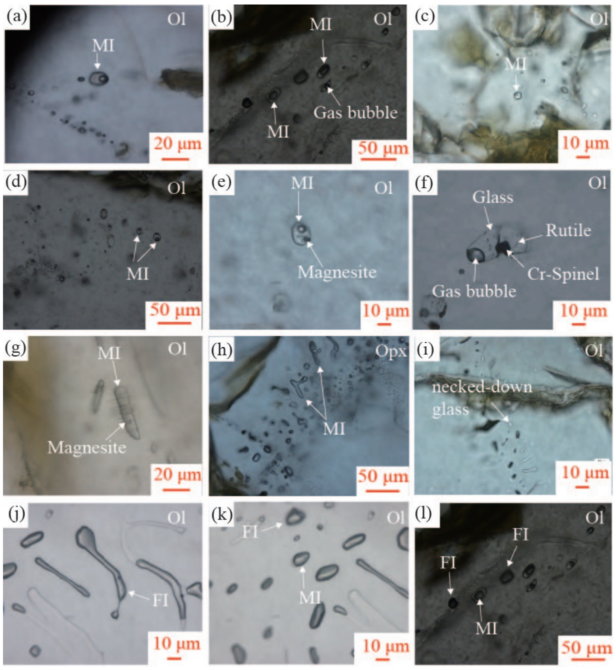

Fig. 5. Photomicrographs of melt inclusions in this study.
(a) Melt inclusions (MI) with elliptical shapes entrapped in olivine. The MI consists of glass and a bubble; (b) ellipse-shaped MI entrapped in olivine. The MI comprises two phases (glass + bubble); (c) rectangular shaped MI entrapped in olivine. The MI consists of glass and a bubble; (d) circular-shaped MI trapped in olivine. The inclusions consist of two phases (glass + bubble); (e–f) elliptically shaped MI entrapped in olivine. The MIs consist of glass, bubble and daughter minerals; (g) elongate MI with neck-down shape entrapped in olivine; (h–i) pure glass MIs distributed in olivine and orthopyroxene; (j–l) fluid inclusions with rounded, elongated and neck-down shapes entrapped in olivine. Images were taken using transmitted light and back-scattered electron imaging.

defined grains of daughter minerals (1 μm in size) and a deformed shrinkage bubble (up to 1–2 μm in size). Daughter crystals in the melt inclusions often have a regular shape. Under cross-polarized light, some daughter phases display high birefringence that is characteristic for carbonates, as identified by Raman spectroscopy.

Melt inclusions are classified petrographically in the same way as fluid inclusions. Based on the relationship between the host mineral and melt inclusions, primary melt inclusions trapped during crystal growth display randomly distributed features. It is noteworthy that the primary melt inclusions do not refer to melt inclusions trapping a primary melt. Secondary melt inclusions grow along healed cracks or cleavage planes, sometimes cutting the boundary minerals (Roedder, 1984). In this study, melt inclusions formed trails along healed fracture planes, and sometimes cut across grain boundaries, suggesting that olivine-hosted melt inclusions in mantle xenoliths are secondary melt inclusions.

2.4 Petrography of fluid inclusions

The olivine-hosted fluid inclusions are also widely distributed in the xenoliths. These fluid inclusions have elongate and irregular shapes, such as tubular, oval-shaped and so on, with a size ranging from 1 to 20 μm in diameter. There are two types of fluid inclusions: one is single phase; the other comprises two phases with a dark appearance at room temperature (Fig. 5j) and is always associated with melt inclusions in the same healed fracture. Sometimes they have a neck-down structure, which indicates that they are genetically associated with the decay of the early fluid inclusions (Fig. 5k–l).

3 Analytical Methods

3.1 Whole-rock major and trace element analyses

Major elements for all samples were determined by X-ray fluorescence (XRF, PW4400) spectroscopy at the National Research Center for Geoanalysis, Chinese Academy of Geological Sciences, Beijing, China. Analyses were performed using fusion beads formed by melting sample powders (200 mesh) with a lithium tetraborate flux. Loss on ignition (LOI) of samples was measured at 1050°C, after drying at 100°C. Relative standard deviations of these analyses are better than 3% for SiO_2, Al_2O_3, Fe_2O_3, MaO, CaO, Na_2O, K_2O and better than 5% for TiO_2, MnO and P_2O_5. Trace element concentrations were measured using an inductively–coupled plasma–mass spectrometer (ICP–MS; PE300Q) following the procedure of Hu et al. (2015). The detection limit for trace element analysis is 0.05 ppm. Analytical uncertainties are <5% for trace elements with concentrations of ≥20 ppm and 5%–10% for elements with concentrations of ≤20 ppm. The detailed analytical methods were described by Liu et al. (2008).

3.2 Major element analyses of olivine and spinel

Olivine grains with spinel inclusions from mantle xenolith samples were analyzed in polished thin-sections by electron microprobe at the Mineral Resources division of the Chinese Academy of Geological Sciences, Beijing, China, using a JEOL–JXA–8230 electron probe micro–analyzer. The analysis was conducted at operating conditions of a 10 μm beam spot for olivine, a 1 μm beam spot for spinel, 40 nA beam current and 15 kV accelerating voltage for olivine and spinel. Peak counting times were 60 s for Al and Cr, 30 s for Ca, Ni and Ti, 10 s for other elements. Natural mineral standards were used for calibration. Under these conditions, the detection limit for Al_2O_3 was <0.007 wt% and the precision was ±0.006 wt% (2σ), based on counting statistics on individual analyses. The detailed analytical methods were described by Wan et al. (2008). The intensity data were corrected using the ZAF method. Melt inclusions and other minerals from xenoliths or xenocrysts were also analyzed in thin-sections using the same EPMA. The detailed analytical methods are the same as above.

3.3 Laser Raman spectroscopy

The composition of melt inclusions (bubbles and daughter minerals) was analyzed by Raman spectroscopy, using a LabRAM HR Evolution (HORIBA Scientific, Paris, France) at the Key Laboratory of Orogenic Belts and Crustal Evolution of the School of Earth and Space Sciences, Peking University. The laser beam had an excitation wave length of 532 nm with a power of 100 mW on the surface of the sample. The diameter of the laser beam was approximately 1000 nm. Individual spectra were obtained with an exposure time of 20 s and a spectral resolution of 2 cm^{-1}. The scanning spectra range was between 100 and 4000 cm^{-1}. Peak positions were determined by fitting according to the Gauss-Lorenz method, the Raman shift being calibrated using monocrystalline silicon as the standard material.

3.4 Mineral trace-element analyses

Trace-element concentrations of pyroxenes were determined by laser ablation-inductively coupled plasma-mass spectrometry (LA-ICP-MS) at the Key Laboratory of Orogenic Belts and Crustal Evolution, MOE, Peking University. Detailed operating conditions for the laser ablation system and the ICP-MS instrument and data reduction were as described by Liu et al. (2008). Laser sampling was performed using a GeoLas 2005. An Agilent 7500a ICP-MS instrument was used to acquire ion-signal intensities. A 'wire' signal-smoothing device was included in this laser ablation system, by which smooth signals were obtained at even very low laser repetition rates, down to 1 Hz (Hu et al., 2015). Nitrogen was added into the central gas flow (Ar + He) of the Ar plasma to decrease the detection limits and improve precision. Each analysis incorporated a background acquisition of 20 s (gas blank) followed by 50 s of data acquisition from the sample. The Agilent Chem–station was utilized for the acquisition of each individual analysis. The preferred values of element concentrations for the U.S. Geological Survey reference glasses are from the GeoReM database (http://georem.mpch–mainz.gwdg.de/). ^{43}Ca was used as the internal standard for clinopyroxene. The accuracy of measurements for the reference materials was better than 10% in relative standard deviation for all elements (rare earth elements (REE), Ti, Sr, and Zr) presented here. Off-line selection and integration of background and analytical signals, as well as time-drift correction and quantitative calibration, were performed by ICPMS-DataCal (Liu et al., 2008).

4 Results

4.1 Major element composition of bulk basaltic rocks and melt inclusions

The 19 samples of late Cenozoic basalts from Hainan Island were analyzed for major and trace element compositions. The results are listed in Supp. Table 1. Loss on ignition (LOI) values of the samples range from 0.03 to 1.65 wt%, resulting from variable amounts of secondarily-altered minerals. After major oxide analyses were re-calculated to 100% on a H_2O and CO_2-free basis (basically represented by LOI in this study), the analyzed samples have SiO_2 of 46.62–50.95 wt%, Al_2O_3 of 14.46–23.27 wt%, Fe_2O_3 of 10.95–12.42 wt%, MgO of 6.24–10.09 wt%. Based on the classification of Le Bas et al. (1986), these basalt samples belong to alkaline and subalkaline series. The alkaline samples are mainly basalt, while the subalkaline samples are mainly basalt and basaltic andesite (Fig. 6).

The compositions for glasses in melt inclusions are listed in Supp. Table 2. The glasses have SiO_2 of 61.94–77.72 wt%, Al_2O_3 of 12.84–14.50 wt%, FeO of 0.52–4.07 wt%, MgO of 0.11–10.41 wt%.

4.2 Trace element composition of bulk basaltic rocks

Trace element analyses for the basaltic samples are listed in Supp. Table 3. On the chondrite-normalized REE

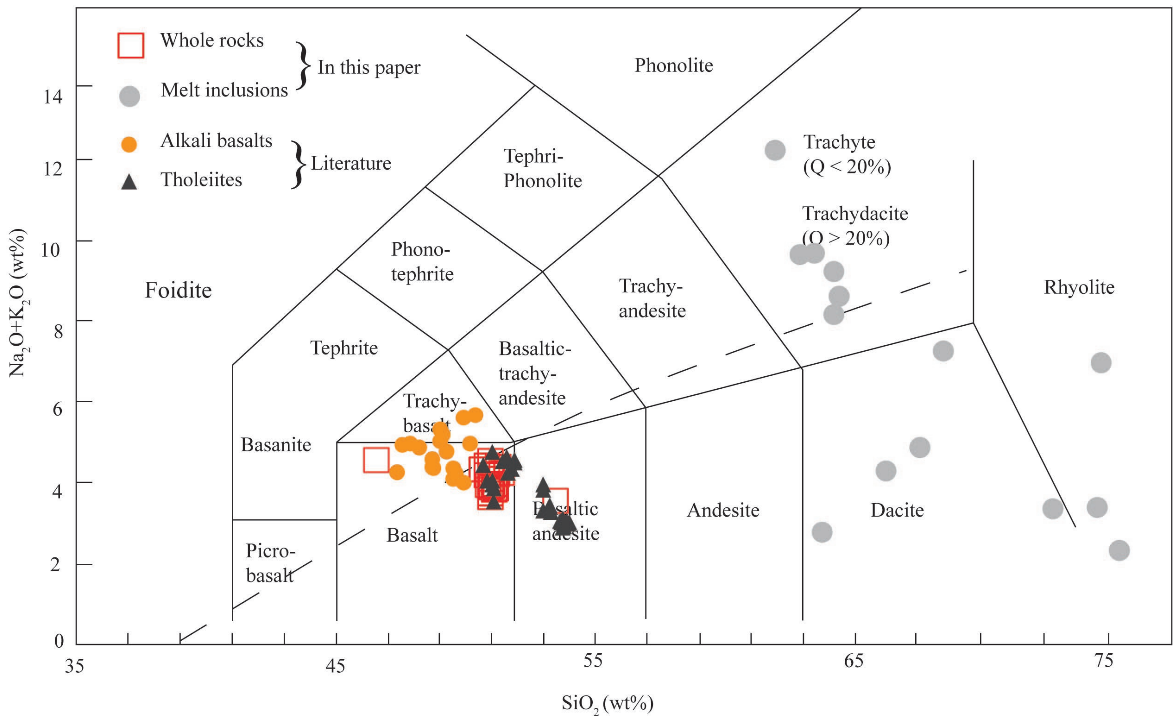

Fig. 6. $Na_2O + K_2O$ versus SiO_2 (Le Bas et al., 1986) for Hainan basalt bulk rock and melt inclusions.
Literature data from Wang et al. (2013), Liu et al. (2015) and Wang et al. (2021).

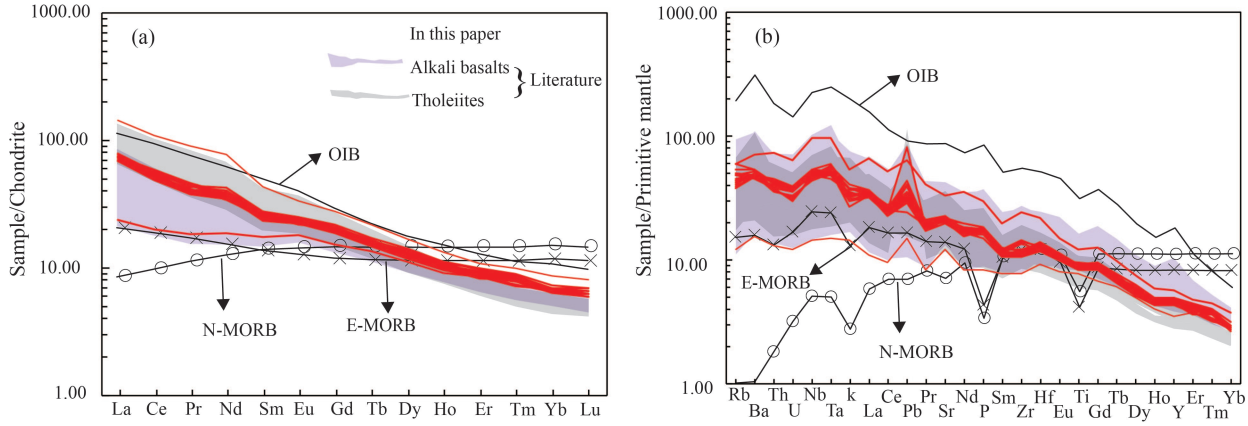

Fig. 7. (a) Chondrite-normalized REE patterns for the late Cenozoic basalts; (b) primitive-mantle normalized trace patterns for the late Cenozoic basalts.
Chondrite, primitive mantle data are from Boynton (1984) and Sun and McDonough (1989), respectively. OIB, N-MORB, E-MORB data from Sun and McDonough (1989). Literature data from Wang et al. (2013, 2021), Liu et al. (2015).

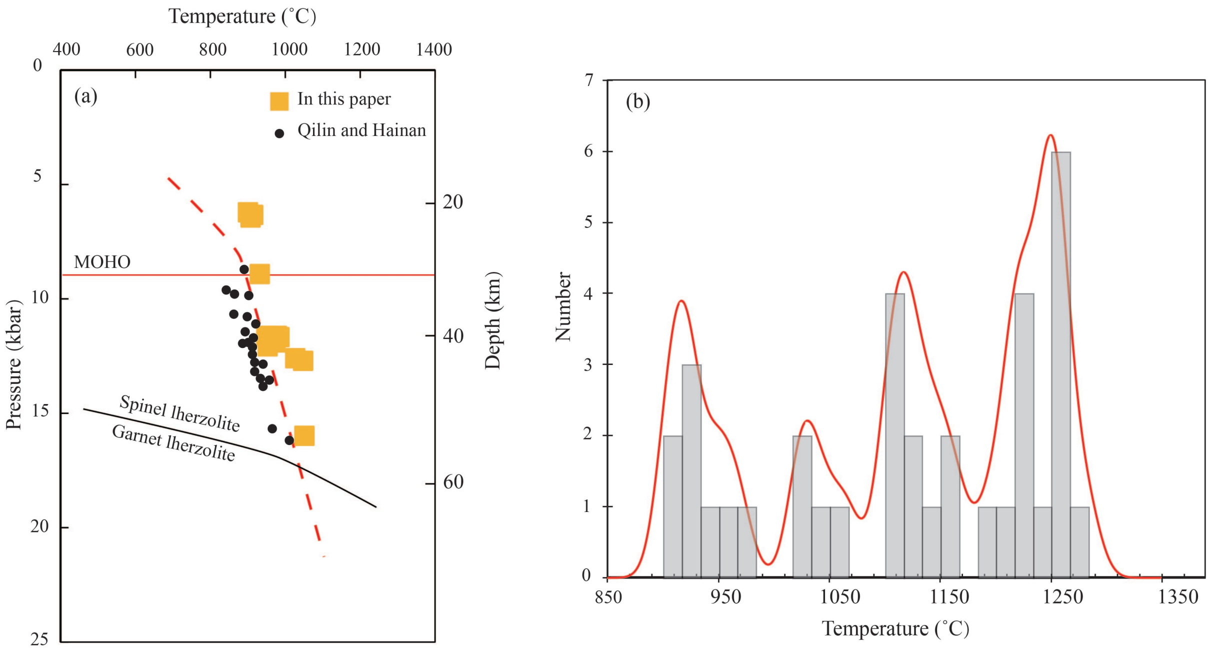

Fig. 8. (a) Geothermal gradient of the lithospheric mantle beneath Hainan Island; Qilin and Hainan data from Xu et al. (2002); (b) histogram showing Al-in-olivine temperatures for mantle xenoliths on Hainan Island.

diagram (Fig. 7a; Boynton, 1984), the samples show fractionated REE patterns with high $(La/Yb)_N$ ratios of 3.52–11.77, typical of OIB. On the primitive mantle-normalized trace element diagram (Fig. 7b; Sun and McDonough, 1989), the samples show positive Rb, Ba, Nb, Ta, Pb and Sr anomalies, with negative Th and U anomalies.

4.3 Pressure-temperature estimation for mantle xenoliths

The depth of Hainan mantle xenoliths trapped by the late Cenozoic basalts is constrained to less than 60 km (c. 20 kbar) by the absence of garnet in the peridotite. We have used the calibration of Nimis and Ulmer (1998) for primary clinopyroxene to estimate the approximate depth of extraction of the lherzolite xenoliths, yielding a pressure range from 6.2 kbar to 16 kbar. Xu et al. (2002) suggested that if the lowest pressure values were less than 9.7 kbar (30 km) for Hainan mantle xenoliths, then they would have been acquired at the shallow lithospheric mantle, near the Moho depth (Fig. 8a).

In this study, we use the Al-in-olivine thermometer to determine the xenolith crystallization temperature, based on the Al-exchange between olivine and spinel, as calibrated experimentally by Wan et al. (2008) and Coogan et al. (2014). The formulation by Coogan et al. (2014) is expressed as:

$$T[°C] = \frac{10^4}{\left[0.575 + 0.884Cr^{\#} - 0.897\ln\left(\frac{Al_2O_3^{ol}}{Al_2O_3^{sp}}\right)\right]} - 273$$

where $Cr^{\#}$ = Cr/(Cr + Al) of spinel calculated in molar units, $Al_2O_3^{ol}$ and $Al_2O_3^{sp}$ are the alumina concentrations (weight percent) in olivines and spinels, respectively, determined by EPMA. The detailed analytical methods were described by Wan et al. (2008). The concentrations of P in olivine are well below 200 ppm. Based on Coogan et al. (2014), the Al distribution between spinel and olivine should not be significantly affected by the Al–P charge balance substitution. The experiments of Wan et al. (2008) and Coogan et al. (2014) had a restricted range of parameters.

A total of 35 points were analyzed for Cr-spinel inclusions in olivine from the Penglai area basalts. All data for olivine and spinel inclusion are listed in Supp. Table 4. Olivine compositions range from Fo 76 to Fo 91. They have Al_2O_3 contents of 0.008–0.035 wt% and NiO contents of 0.19–0.44 wt%. The olivine crystals show a relatively positive correlation between Al_2O_3 and Fo contents. Spinels are Cr-rich and exhibit $Cr^{\#}$ of 0.14–0.71 and Al_2O_3 of 5.83–52.89 wt%. For this reason, spinels with Fe^{3+}/Fe^{total} = 0–0.35 and $Cr^{\#}$ = 0–0.69 (Cr/(Cr + Al)) were used to obtain reliable results from the Al–in–olivine thermometer. The calculated crystallization temperatures for the xenoliths of the Penglai area basalts range from 905°C to 1282°C (Fig. 8b; Supp. Table 4), with the average value being 1117°C. The intrinsic error of the thermometer is estimated to be within ± 25°C (Coogan et al., 2014).

We also used the Ca-in-Opx thermometer of Brey & Köhler (1990) and the pyroxene thermometer from Wells (1977) and Wood & Banno (1973) to estimate the temperature of mantle xenoliths in northern Hainan Island (Table 1). The estimated values from the three different geological thermometers are 901–1052°C, 924–997°C and 1027–1089°C, respectively. Xu et al. (2002) used the Brey & Köhler (1990) Ca-in-Opx thermometer to calculate the equilibrium temperature of Hainan spinel lherzolite. Their results show that the equilibrium temperature of Hainan mantle xenoliths is 800–1080°C. Based on the Brey and Köhler (1990) Ca-in-Opx thermometer (error is ±60°C), Jiang et al. (2017) calculated the equilibrium temperatures for three types of lherzolites in Hainan, the results being 818–1015°C, 960–977°C, 864–988°C. The average equilibrium temperature of lherzolites is 932°C.

Table 1 Estimated results of mantle peridotite temperature (°C) in northern Hainan Island

Sample	Brey and Köhler (1990)	Wells (1977)	Wood and Banno (1973)
PL13–1	975	954	1045
PL13–2	955	942	1034
PL13–3	952	937	1032
PL13–4	1049	991	1058
PL13–5	988	956	1038
PL13–6	979	—	—
PL6–1	901	932	1035
PL6–2	917	932	1033
PL6–3	909	924	1027
PL23a–1	1029	997	1089
PL13–33b–1	932	943	1039
PL13–33b–2	1052	989	1085

T_{BKCa}–Brey and Köhler (1990) Ca-in-Opx thermometer; T_W–Wells (1997) thermometer; T_{WB}–Wood and Banno (1973) thermometer.

4.4 Mineralogical features in the mantle xenoliths

4.4.1 Olivine

The olivine $Mg^{\#}$ ($Mg^{\#}_{ol}$ = 100 × $Mg^{2+}/(Mg^{2+} + Fe^{2+})$) value is between 86 and 91. The data are listed in Supp. Table 5A. Based on the $Mg^{\#}_{ol}$ value, the olivines can be divided into three types. Samples with high $Mg^{\#}_{ol}$ value (>90), are classified as relatively refractory mantle peridotite. Samples with $Mg^{\#}_{ol}$ values of 87–90 represent fertile mantle peridotite. The third type of mantle peridotite has low $Mg^{\#}_{ol}$ values (<87). The three types of peridotites all belong to spinel lherzolites. Olivines from mantle xenoliths have CaO content of 0–0.14 wt%, NiO content of 0.27–0.50 wt% and MnO content of 0.06–0.18 wt%. Generally, magmatic olivine has CaO > 0.1 wt% and MnO > 0.2 wt%. Fig. 9 shows these olivine compositions

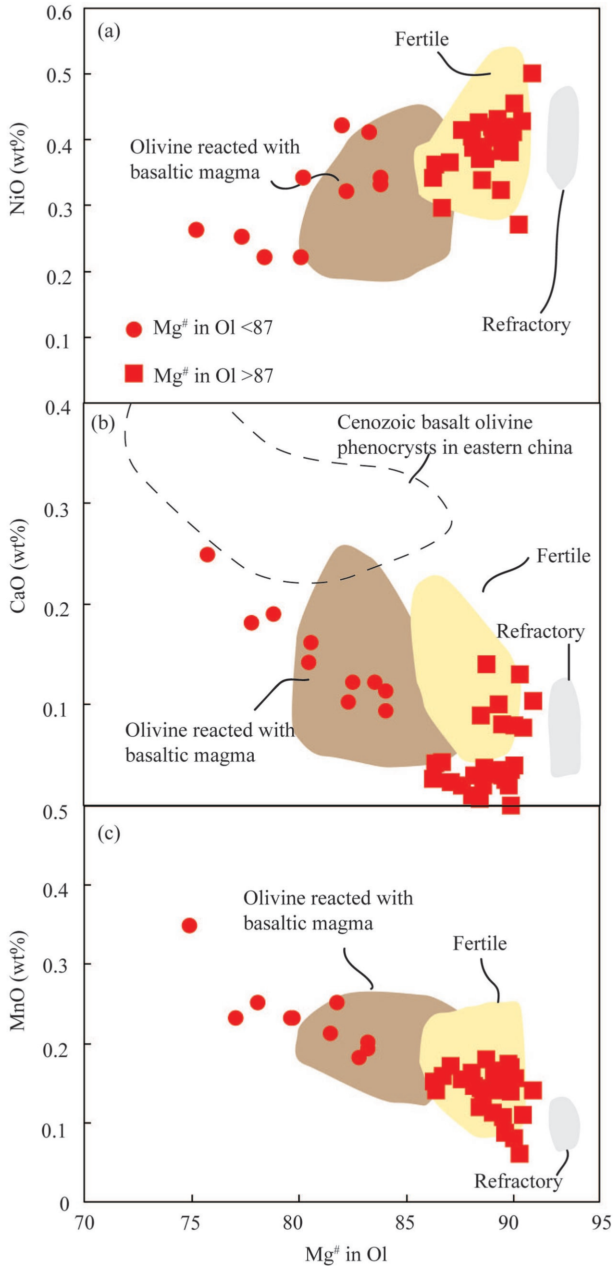

Fig. 9. Relationship of $Mg^{\#}$ in olivine vs. NiO, CaO, MnO.

basically falling in the range for 'fertile peridotite', representing a juvenile lithospheric mantle. In addition, the olivine xenocrysts of sample PL–13 have $Mg^{\#}_{ol}$ varying from 84 to 75 from core to rim. The content of other elements in olivine with banding also changes significantly. For example, from the core to the rim, the contents of MgO, NiO and SiO_2 decreases gradually, while the contents of CaO and FeO increases gradually (Fig. 10). The olivine xenocrysts are similar to olivine phenocrysts of basalt in eastern China in their geochemical characteristics.

4.4.2 Orthopyroxene

The $Mg^{\#}_{opx}$ value ($Mg^{\#}_{opx} = 100 \times Mg^{2+}/(Mg^{2+} + Fe^{2+})$) of orthopyroxenes in this study ranges from 86 to 92. The data are listed in Supp. Table 5B. Relatively high $Mg^{\#}_{opx}$ value (>90), medium $Mg^{\#}_{opx}$ value (87 to 90) and low $Mg^{\#}_{opx}$ value (<87), correspond to refractory peridotite, fertile peridotite and peridotite reacted with basaltic magma. These orthopyroxenes contain Al_2O_3 (1.07–4.56 wt%), Cr_2O_3 (0.022–0.686 wt%) and NiO (0.04–0.19 wt%). As can be seen from Fig. 11, these orthopyroxenes basically fall into the range for 'fertile peridotite', representing the juvenile lithospheric mantle.

4.4.3 Clinopyroxene

In general, the compositional characteristics of

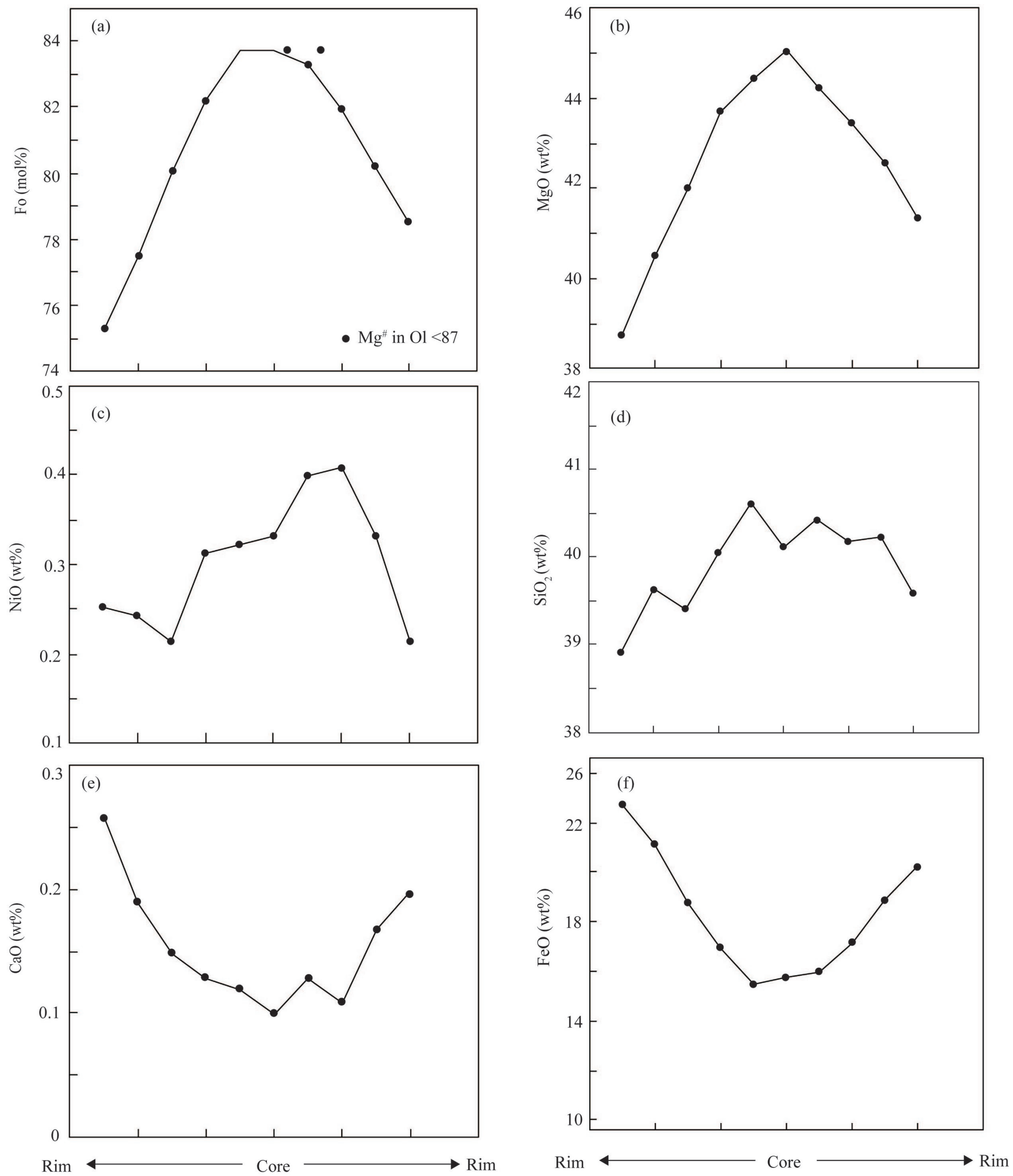

Fig. 10. Diagram of Fo, CaO, NiO, MgO, FeO, SiO_2 contents changing from core to rim.

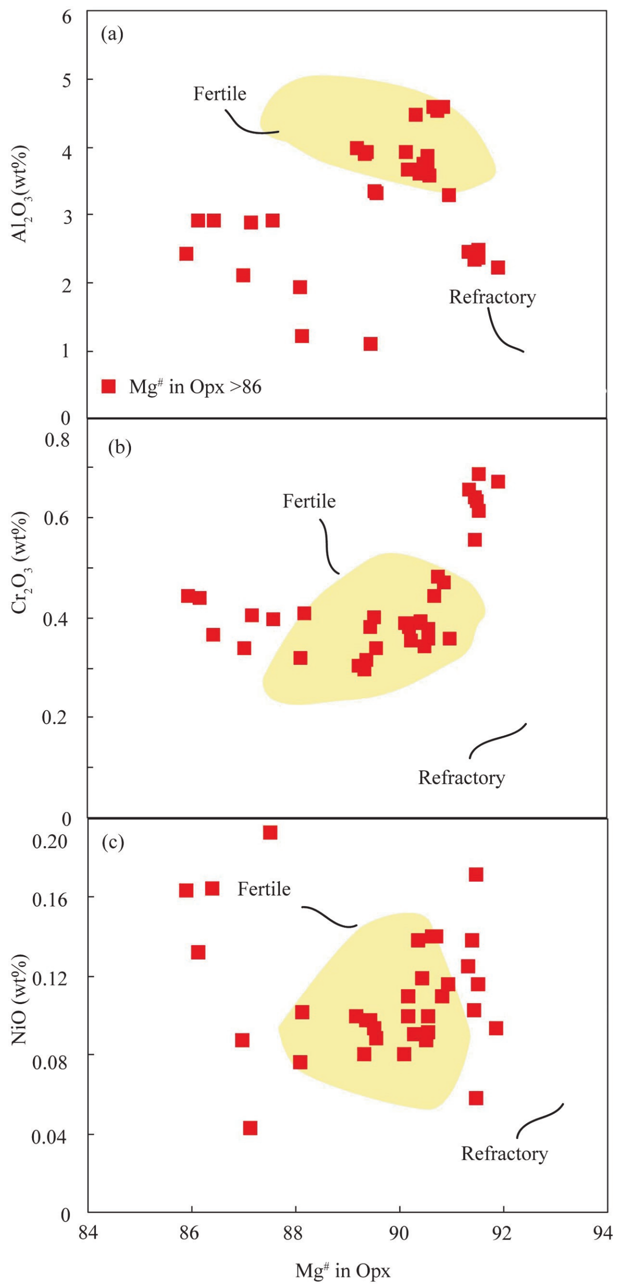

Fig. 11. Relationship of $Mg^{\#}$ in orthopyroxene vs. Al_2O_3, Cr_2O_3, NiO.

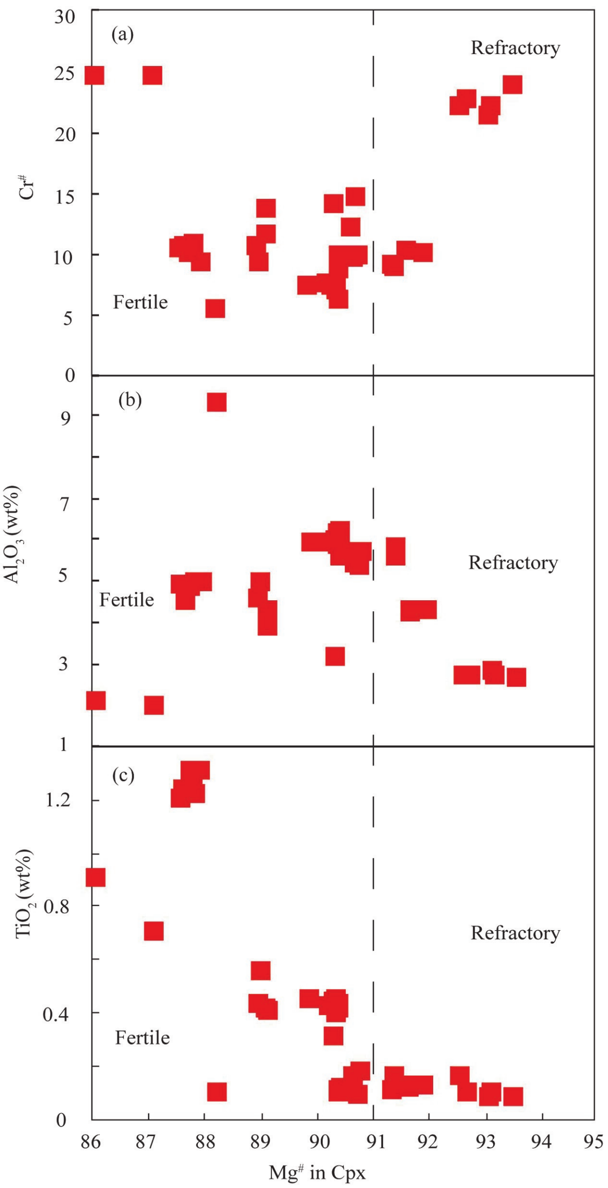

Fig. 12. Relationship of $Mg^{\#}$ in clinopyroxene vs. $Cr^{\#}$, Al_2O_3, TiO_2.

clinopyroxene in mantle peridotites are of great importance for discussing the origin and evolution of the lithospheric mantle. The data for clinopyroxene composition are listed in Supp. Table 5C. Clinopyroxenes in the first type of mantle peridotite have relatively high $Mg^{\#}_{cpx}$ values (92–94), $Cr^{\#}$ values ($Cr^{\#} = 100 \times Cr/(Cr + Al)$) of 10–24 and Al_2O_3 contents of 2.62–4.28 wt%. Previous studies have found that refractory clinopyroxenes of mantle peridotite in the Archean lithosphere residue in the Hebi area of the North China Craton have $Cr^{\#}$ values greater than 10 and $Mg^{\#}_{cpx}$ values more than 91 (Li, 2015). According to the chondrite-normalized REE diagram, clinopyroxene in the first type of relatively refractory mantle peridotite is depleted in LREE and enriched in HREE, $(La/Yb)_N$ = 0.18–0.30 (Figs. 12, 13a). On the primitive-mantle normalized trace element diagram, the content of incompatible elements in clinopyroxene is relatively low, with positive anomalies of Th, U and Sr, as well as negative anomalies of Ba, Nb, Ta, Zr and Hf (Fig. 13b). The clinopyroxene in the first type of relatively refractory mantle peridotite in Hainan Island, has similar geochemical characteristics to that of the clinopyroxene in the mantle peridotite in the Hebi area of the North China Craton. Clinopyroxene in the second type of fertile mantle peridotite has moderate $Mg^{\#}_{cpx}$ value (90–91), $Cr^{\#}$ value between 7–15, and Al_2O_3 content of 5.38%–6.21%. According to the chondrite-normalized REE diagram of clinopyroxene, the second type of fertile mantle peridotite clinopyroxene has a U-shaped distribution, with the highest LREE content and relatively flat HREE content,

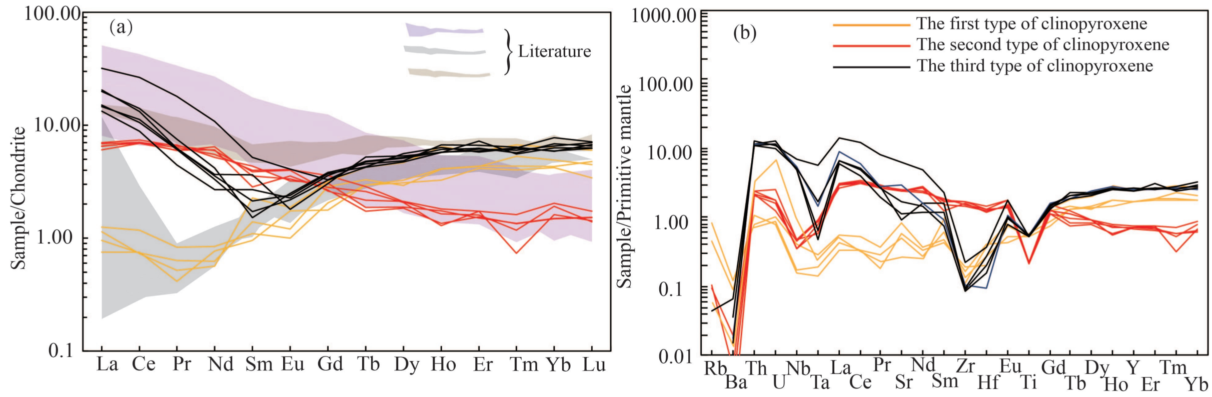

Fig. 13. (a) Chondrite-normalized REE patterns for the late Cenozoic basalts; (b) primitive mantle-normalized trace patterns for the late Cenozoic basalts.
Chondrite, primitive mantle data are from Boynton (1984) and Sun and McDonough (1989), respectively. Literature data from Jiang et al. (2017).

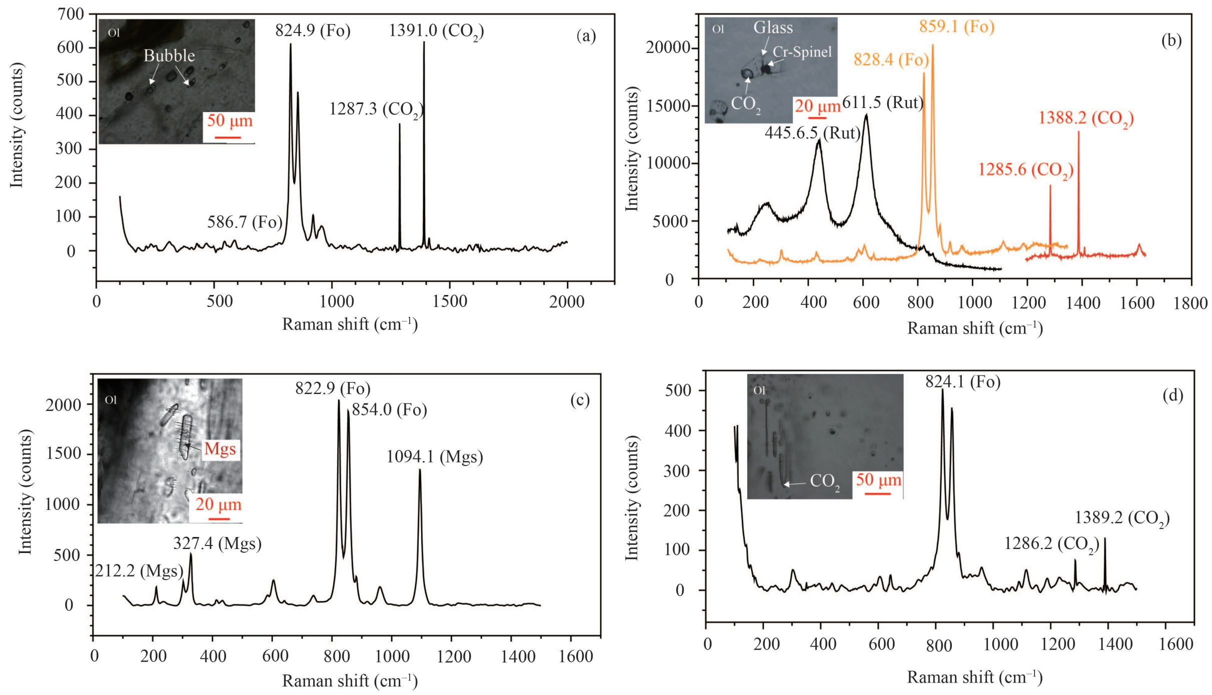

Fig. 14. Summary of representative Raman spectra of MI at room temperature.
(a) Laser Raman spectrum of the bubbles in MI; (b) Laser Raman spectrum of bubble, daughter minerals in MI; (c) Laser Raman spectrum of daughter mineral in MI; (d) Laser Raman spectrum of CO_2 dissolved in glass. Fo–olivine; Rut–rutile; Mgs–magnesite.

$(La/Yb)_N$ = 1.96–4.12 (Figs. 12, 13a). On the primitive-mantle normalized trace element diagram, the content of incompatible elements in clinopyroxene is relatively high, with positive anomalies of Th, U and Sr, alongside negative anomalies of Ba, Nb, Ta, Zr and Hf (Fig. 13b). The third type of mantle peridotite clinopyroxene has $Mg^{\#}_{cpx}$ values from 86 to 89 and $Cr^{\#}$ values between 5 and 13 (excluding two samples with $Cr^{\#}$ value of 24) and Al_2O_3 content of 3.90–4.97 wt% (excluding two samples with Al_2O_3 values of 1.95 and 2.11). According to the chondrite-normalized REE diagram of clinopyroxene, clinopyroxene in the third type of relatively refractory mantle peridotite is enriched in LREE, has a right-dipping feature of HREE and relative depletion of $(La/Yb)_N$ = 0.18 –4.36 (Figs. 12, 13a). On the primitive-mantle normalized trace element diagram, the clinopyroxene has medium content of the incompatible elements, with positive anomalies of Th, U and Sr, alongside negative anomalies of Ba, Nb, Ta, Zr and Hf (Fig. 13b).

4.5 Raman spectroscopy of silicate melt inclusions

Laser Raman analyses of MI suggested that the volatile components in the MI are dominated by CO_2. The results of Laser Raman analyses of MI are shown in Fig. 14. The Raman spectrum shows the olivine–host, with Raman shifts at 825 and 855 cm^{-1} (Fig. 14a–d). The Raman spectra of the bubbles in MI show two strong bands at 1285 and 1388 cm^{-1}, which are characteristic for molecular CO_2, indicating the bubbles in MI are mainly CO_2 (Frezzoti et al., 2012; Fig. 14a–b, d). In Fig. 14d, peaks at 1286.2 cm^{-1} and 1389.2 cm^{-1} are very weak, suggesting low CO_2 concentrations in MI. The daughter mineral in Fig. 14b is rutile, with characteristic peaks at 445.6 cm^{-1} and 611.5 cm^{-1}. In addition, the Cr-spinel was identified by EPMA (Fig. 14b). Magnesite was also detected in several melt inclusions, which has Raman shifts at 327.4 and 1094 cm^{-1} (Fig. 14c).

5 Discussion

5.1 Crustal contamination

Compared to oceanic island basalts, continental intra–plate basalts are expected to pass the thick continental crust before eruption. As such, it is necessary to evaluate the influence of crustal contamination. O'Reilly and Griffin (2010) suggested that if mantle xenoliths are hosted in magma, the magma possibly spent 8–60 h travelling from the depth of 80–200 km to the surface. In the study area, there are many mantle xenoliths and xenocrysts in the Hainan basalts (Fan and Hooper, 1989; Xu et al., 2002; Liu et al., 2015; Jiang et al., 2017), indicating that magma ascended rapidly, without enough time to assimilate the crust (Liu et al., 2015; Sun et al., 2018; Lei et al., 2021).

In addition, continental crust material displays the features of relatively high SiO_2 and low MgO, with enrichment in LILEs (e.g., Rb, Ba, U and K) and depletion in HFSEs (e.g., Nb, Ta and Ti). The Hainan basalts have SiO_2 of 46.62–53.79 wt%, MgO of 6.24–10.09 wt% and positive Nb and Ta anomalies as shown in Fig. 7b. Furthermore, oceanic basalts (MORB and OIB) have average Ce/Pb and Nb/U ratios of 25 ± 5 and 47 ± 7, respectively (Hofmann et al., 1986), distinctly higher than that of continental crust (4.8 and 7.4, respectively, Taylor, 1964; 6.15 and 3.91, respectively, Rudnick and Gao, 2003). In contrast, Ce/Pb and Nb/U in the Hainan basalts range from 15.67 to 26.64 and from 40.40 to 51.16, respectively. These values are much closer to the average ratios of oceanic basalts. Th/Ta (1.57–1.82) and Nb/La (1.37–1.57) in the Hainan basalts plot between the OIB and primitive mantle, suggesting that crustal material was not added into the basaltic magma. This is consistent with the fact that the late Cenozoic basalts, in the whole South China Sea and its surrounding areas, are hardly contaminated by crustal materials. Recently, Zou and Fan (2010) indicated that Hainan basalts have a ^{230}Th excess, which excludes crustal contamination. Thus, the above evidence indicates that crustal contamination plays an insignificant role in the petrogenesis of these basalts (Wang et al., 2012, 2013).

5.2 Partial melting in the lithospheric mantle

Mantle xenoliths provide a window for investigating the lithospheric mantle and deep processes such as melt extraction and mantle metasomatism. In the long history of geological evolution, the lithospheric mantle has experienced multiple periods of melt extraction, resulting in mantle-derived magmas. Fusible components such as Al, Fe, Ti, etc., are easy to extract. Generally speaking, with a higher degree of extraction, the peridotite is more 'refractory', otherwise it is characterized as 'fertile'. Olivine $Mg^{\#}$ values and clinopyroxene $Mg^{\#}$ values can usually be used to reflect the extraction degree of the melt and also show the 'refractory' and 'fertile' degrees of the mantle xenoliths. The correlations between $Mg^{\#}$ values of olivine, orthopyroxene, clinopyroxene and other elements show that mantle peridotite has experienced the process of melt extraction (Figs. 9–11). In mantle peridotite, clinopyroxene is generally the main carrier of trace elements and the most important mineral (Li, 2015).

There are two principal methods for calculating the degree of mantle melting: the first is to use the major elements of minerals for calculation. The formula established by Hellebrand et al. (2001), $F = 10 \times \ln (Cr^{\#}) + 24$ (where the $Cr^{\#}$ value in spinel is between 0.1 and 0.6), is used to obtain the estimate of the Hainan Island mantle peridotite that represents the residue after 15%–22% melt extraction. The second method is to use the relationship between the mineral trace elements to determine the melting degree of the mantle peridotite. Johnson et al. (1990) and Norman (1998) established the covariant relationship between Yb_N and Y_N in clinopyroxene under batch melting and fractional melting conditions. Based on the parameters given by Norman (1998), $D_Y^{Cpx/melt} = 0.42$, $D_{Yb}^{Cpx/melt} = 0.40$, Fig. 15a, b simulate the changes of clinopyroxene Y and Yb contents in batch melting and fractional melting scenarios, respectively. Fig. 15a shows

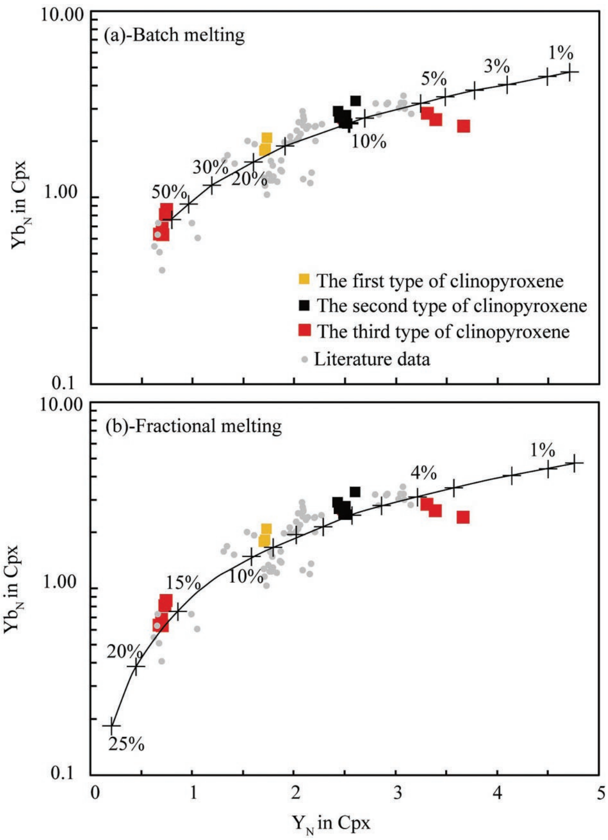

Fig. 15. (a) Batch melting and (b) fractional melting modes with the primitive mantle-normalized Yb and Y in clinopyroxene from Hainan Island mantle xenoliths, assuming a primitive mantle source.

Literature data from Jiang et al. (2017).

that some mantle peridotites from northern Hainan Island need to undergo about 50% batch melting to be in accord with the content of rare earth elements in clinopyroxene. According to Zimbelman and Gregg (2000), if the mantle undergoes more than 40% partial melting, it will form komatiite, which is inconsistent with the actual observations. Fig. 15b shows that using a fractional melting model, the samples basically fall on the trend line, suggesting that the mantle peridotites in Hainan Island come from the spinel-stable zone, with a partial melting degree of 4%–20%. the partial melting degree for the first type clinopyroxene being about 9%, the partial melting degree for the second type clinopyroxene being about 6% and the partial melting degree of the third type clinopyroxene being 3%–20%. It is similar to the method of estimating the partial melting degree of the mantle by using spinel $Cr^{\#}$.

5.3 Implications for mantle metasomatism

Mantle metasomatism refers to the interaction between the silicate/carbonate melts or fluid and mantle, resulting in the change of mantle chemical compositions and properties. The metasomatism can be divided into modal metasomatism and cryptic metasomatism, respectively (Harte, 1983; Dawson, 1984). Metasomatic minerals (phlogopite, amphibole, etc.) are not found in the mantle peridotite in northern Hainan Island. In Fig. 13, both chondrite-normalized REE diagram and the primitive-mantle normalized trace element diagram show that the second and third types of clinopyroxene are obviously enriched in light rare earth elements (LREE) and other trace elements, which indicates that the peridotite has undergone cryptic metasomatism. Compared with the other two types, the first type of clinopyroxene has low contents of light rare earth elements (LREE) and large ion lithophile elements (LILE). Low degree mantle metasomatism and early metasomatism with strong incompatible elements (Th, U, Sr, etc.) occurred in the first type of clinopyroxene. The second type of clinopyroxene has high contents of LREE and LILE, with positive Th and U anomalies and negative Rb, Ba, Nb, Ta, Sr anomalies, suggesting that the metasomatic agent has relatively high contents of LREE and incompatible elements such as Th and U. The third type of clinopyroxene has medium contents of LREE and LILE, with positive Th and U anomalies and negative Rb, Ba, Nb, Ta, Sr anomalies, suggesting that the metasomatic agent contains moderate LREE and incompatible elements such as Th and U. Above all, the first type of clinopyroxenes has very low Sr, Nb, La and Zr contents, indicating that they have experienced a very low degree of mantle metasomatism. However, the second and third types of clinopyroxenes have higher Sr, Nb, La and Zr contents than the first type of clinopyroxenes, indicating that they have experienced strong metasomatism.

The metasomatic agent is melt rather than fluid, because the solubility of Nb, Zr in aqueous fluids is extremely low, but their solubility is high in silicate melts or carbonate melts with a large wetting dihedral angle (Keppler, 1996). Fig. 7b shows that the trace elements in the whole rock of late Cenozoic basalts have positive Nb and Ta anomalies, but the Nb and Ta anomalies in mantle xenoliths are negative (Fig. 13b). Therefore, we speculate that the metasomatic agent comes not from the host basaltic magma, but from other materials in the lithospheric mantle.

Compared with silicate melt metasomatism, carbonate melt metasomatism will cause clinopyroxene to have relatively high Ca and low Al content (Fig. 16a, b). In carbonate melts, it is easier for Ti to enter clinopyroxene (Rudnick et al., 1993). Therefore, we use the the Ti/Eu ratio to trace the metasomatism of carbonate melts. Carbonate melts are enriched in LREE and metasomatized clinopyroxene will have higher $(La/Yb)_N$ ratios. By simulating mantle conditions, Coltorti et al. (1999) suggested that if the carbonate melts replaced clinopyroxene, the $(La/Yb)_N$ ratio of clinopyroxene is usually greater than 3–4 and the Ti/Eu ratio is less than 1500. Zong and Liu (2018) believed that the above ratios are not an absolute standard, the authors suggesting that it would be more reasonable to use the trend defined by the ratios. Clinopyroxene $(La/Yb)_N$–Ti/Eu and clinopyroxene Ca/Al–$Mg^{\#}$ are usually used to distinguish silicate melt metasomatism and carbonate melt metasomatism (Fig. 16c, d). A part of the clinopyroxene samples in mantle peridotite plot in the silicate melt metasomatism area; while others fall into the carbonate melt metasomatism area, indicating that the mantle peridotite experienced the metasomatism of melts of different compositions.

In summary, we propose that the lithospheric mantle of Hainan Island has experienced both silicate melt and carbonate melt metasomatism.

5.4 CO_2 entrapment in the lithospheric mantle

The Hainan Island mantle xenoliths have undergone silicate melt metasomatism, as indicated by a large number of Si-rich melt inclusions developed in the mantle peridotites (Xu et al., 2002; Wu et al., 2005; Wang et al., 2012). Melt inclusions in spinel lherzolite provide direct evidence for discussing the type of metasomatic agent in the lithospheric mantle. We chose olivine-hosted melt inclusions as a research object. Based on the electron microprobe analysis, the glasses in olivine-hosted melt inclusions have a high content of SiO_2 (60.21–77.72 wt%), which precludes a genetic relationship between the melt inclusions and the host basaltic magma. Based on the thin-section observations, melt inclusions mostly cut through the mineral boundaries, indicating that melt inclusions are secondary, eliminating the possibility that melt inclusions result from the partial melting of host minerals (Chazot et al., 1996). Melt inclusions are not generated by melting of the hydrous minerals, because phlogopite and amphibole are not found in the peridotite (Ionov et al., 1994). Therefore, olivine-hosted melt inclusions may represent part of a migrating silicate melt phase in the lithospheric mantle (Schiano and Clocchiatti, 1994).

Carbonates are observed in the melt inclusions and the carbonate phase distributes across the glass–bubble interface in the form of tiny crystals, rather than as a single, large crystal. Laser Raman analyses of MI suggest that the tiny solid components in the MI are magnesite (Fig. 5e, g), Ionov et al. (1993) in turn suggesting that

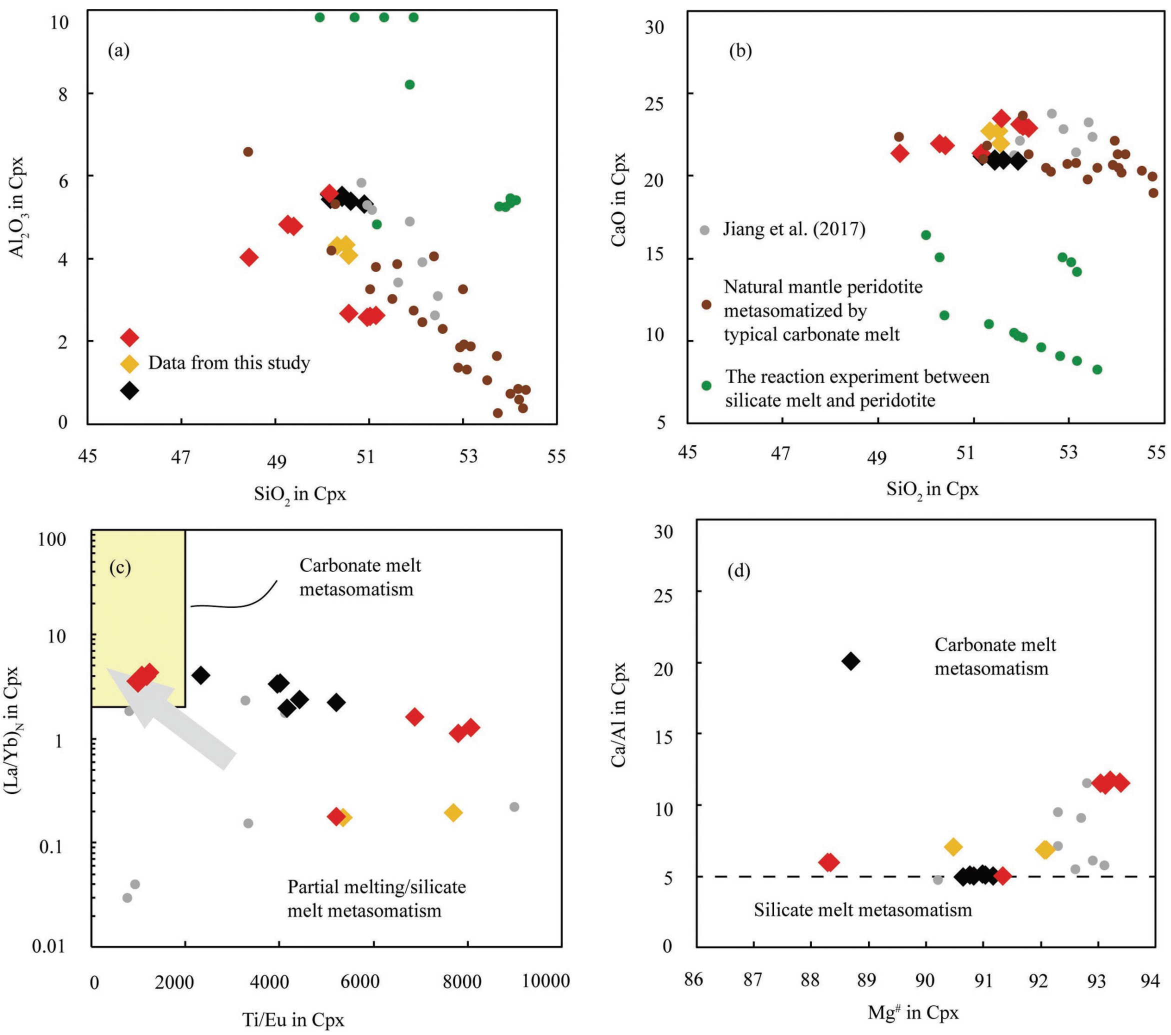

Fig. 16. (a) Relationship of SiO_2 in Cpx vs. Al_2O_3 in Cpx; (b) relationship of SiO_2 in Cpx vs. CaO in Cpx; (c) relationship of Ti/Eu in Cpx vs. $(La/Yb)_N$ in Cpx; (d) relationship of $Mg^{\#}$ in Cpx vs. Ca/Al in Cpx.
The reaction experiment between silicate melt and peridotite data from Wang et al. (2010), Yaxley and Green (1998); natural mantle peridotite metasomatized by typical carbonate melt data from Yaxley and Green (1998), Neumann et al. (2002). The clinopyroxene in Hainan mantle xenoliths data is from Jiang et al. (2017).

partial melting of a carbonated peridotite may form magnesite in melt inclusions. If this is true, not only does partial melting of carbonated peridotite produce carbonates, but also an Al, Na-rich mafic silicate glass in peridotite. However, the silicate glass in our melt inclusions is felsic in composition. Therefore, the magnesite cannot be formed by partial melting of carbonated peridotite. Moore et al. (2015) suggested that carbonates were commonly identified in the MI because of the reaction between the CO_2 in the fluid and surrounding melts. In this study, we suggest that magnesites in MI could be interpreted as a secondary mineral, formed by interactions of CO_2-rich fluids with olivine (Frezzotti et al., 2002; Moore et al., 2015; Wallace et al., 2015; Tucker et al., 2019; Weiser et al., 2020). Mg, such as Mg^{2+}, precipitates due to reaction with CO_3^{2-} in the fluid at specific temperatures. Experimental studies have shown that CO_2-saturated fluid can easily form magnesite by reacting with olivine (Kwak et al., 2011; Schaef et al., 2013; Loring et al., 2015; Stopic et al., 2018). The daughter minerals of type II MI (glass + CO_2 bubble + daughter minerals) illustrate a characteristic paragenesis. To explain the needle-like rutile in olivine-hosted MI in mantle xenoliths, Schiano and Clocchiatti (1992) proposed a metasomatic mechanism theory, the authors suggesting that a change in the fO_2 resulted in the precipitation of Ti in the form of needle-like rutile. The appearance of Cr-spinel is caused by immiscibility during the cooling of the melt. Melt inclusions (CO_2 + glass) and fluid inclusions (CO_2-dominated inclusions) occur together along healed fractures in the olivine of mantle xenoliths, relative to olivine formation (as secondary inclusions, Fig. 5k, l). The coexistence of melt inclusions and fluid inclusions in the olivine of mantle xenoliths indicates that these inclusions formed by the immiscible mixture of silicate melt and CO_2 under lithospheric mantle conditions. The presence of CO_2 in type I MI (CO_2 bubble-rich melt inclusions) and type II (glass + bubble + daughter minerals) has been identified by Laser Raman analyses of shrink bubbles, indicating that CO_2 oversaturation in the melt occurred under conditions of temperature and pressure corresponding to the entrapment event.

In summary, a considerable amount of CO_2-rich melt inclusions are captured in the lithospheric mantle during the metasomatic process.

6 Conclusions

Olivine-hosted melt inclusions occur commonly in Hainan Island spinel lherzolites and the volatile components in the melt inclusions are dominated by CO_2. Magnesite in melt inclusions could be interpreted as a secondary mineral formed by interactions of CO_2-rich fluids with the olivine host due to post-entrapment effects. Some of the clinopyroxene samples in mantle peridotite from northern Hainan Island fall into the silicate melt metasomatism area, while others fall into the carbonate melt metasomatism area, indicating that the lithospheric mantle has undergone metasomatism through melts of different compositions. A considerable amount of CO_2-rich melt inclusions are captured in the lithospheric mantle during the process of metasomatism. These results imply that lithospheric mantle is a 'carbon trap' and that considerable CO_2 can be absorbed by the lithospheric mantle.

Acknowledgments

This work is supported by the National Key Research and Development Project (Grant. No. 2019YFA0708503).

Manuscript received Oct. 30, 2022
accepted Jan. 20, 2023
associate EIC: ZHANG Lifei
edited by Jeffery J. LISTON and FANG Xiang

References

Anderson, A.T., Davis, A.M., and Lu, F.Q., 2000. Evolution of Bishop Tuff rhyolitic magma based on melt and magnetite inclusions and zoned phenocrysts. Journal of Petrology, 41: 449–473.

Aster, E.M., Wallace, P.J., Moore, L.R., Watkins, J., Gazel, E., and Bodnar, R.J., 2016. Reconstructing CO_2 concentrations in basaltic melt inclusions using Raman analysis of vapor bubbles. Journal of Volcanology and Geothermal Research, 323: 148–162.

BGGP (Bureau of Geology, Guangdong Province), 1964. Hainan Island sheet regional (1: 200000). Geological Survey Report (in Chinese).

Bodnar, R.J., and Student, J.J., 2006. Melt inclusions in plutonic rocks: Petrography and micro thermometry. In: Webster, J.D. (ed.), Melt Inclusions in Plutonic Rocks. Mineralogical Association of Canada, Short Course 36: 1–26.

Boynton, W.V., 1984. Cosmochemistry of the rare earth elements: Meteorite studies. In: Henderson, P., (ed.), Rare Earth Element Geochemistry, Developments in Geochemistry No. 2. Amsterdam: Elsevier, 63–114.

Brey, G.P., and Köhler, T., 1990. Geothermobarometry in Four-phase Lherzolites II. New Thermobarometers, and Practical Assessment of Existing Thermobarometers. Journal of Petrology, 31: 1353–1378.

Bucholz, C.E., Gaetani, G.A., Behn, M.D., and Shimizu, N., 2013. Post-entrapment modification of volatiles and oxygen fugacity in olivine-hosted melt inclusions. Earth and Planetary Science Letters, 374: 145–155.

Chazot, G., Menzies, M. and Harte, B., 1996. Silicate glasses in spinel lherzolites from Yemen: Origin and chemical composition. Chemical Geology, 134: 159–179.

Chung, S.L., Cheng, H., Jahn, B.M., O'Reilly, S.Y., and Zhu, B.Q., 1997. Major and trace element, and Sr-Nd isotope constraints on the origin of Paleogene volcanism in South China prior to the South China sea opening. Lithos, 40: 203–220.

Coltice, N., Simon, L., and Lecuyer, C., 2004. Carbon isotope cycle and mantle structure. Geophysical Research Letters, 31: 1–5.

Coltorti, M., Bonadiman, C., Hinton, R.W., Siena, F., and Upton, B.G.J., 1999. Carbonatite metasomatism of the oceanic upper mantle: Evidence from clinopyroxenes and glasses in ultramafic xenoliths of Grande Comore, Indian Ocean. Journal of Petrology, 40: 133–165.

Coogan, L.A., Saunders, A.D., and Wilson, R.N., 2014. Aluminum–in–olivine thermometry of primitive basalts: Evidence of an anomalously hot mantle source for large igneous provinces. Chemical Geology, 368: 1–10.

Danyushevsky, L.V., McNeill, A.W., and Sobolev, A.V., 2002. Experimental and petrological studies of melt inclusions in phenocrysts from mantle-derived magmas: An overview of techniques, advantages and complications. Chemical Geology, 183: 5–24.

Dasgupta, R., and Hirschmann, M.M., 2010. The deep carbon cycle and melting in Earth's interior. Earth and Planetary Science Letters, 298: 1–13.

Dawson, J.B., 1984. Contrasting types of upper mantle metasomatism? In: Kornprobst, J. (ed.), Kimberlites II. The Mantle and Crust/Mantle Relationships. Amsterdam: Elsevier, 289–294.

Dixon, J.E., Stolper, E.M., and Holloway, J.R., 1995. An experimental study of water and carbon dioxide solubilities in mid-ocean ridge basaltic liquids. Part I: Calibration and Solubility Models. Journal of Petrology, 36: 1607–1631.

Esposito, R., Bodnar, R.J., Danyushevsky, L.V., De Vivo, B., Fedele, L., Hunter, J., Lima, A., and Shimizu, N., 2011. Volatile evolution of magma associated with the Solchiaro eruption in the Phlegrean Volcanic District (Italy). Journal of Petrology, 52: 2431–2460.

Fan, Q.C., and Hooper, P.R., 1989. The mineral chemistry of ultramafic xenoliths of eastern China: Implications for upper mantle composition and the paleogeotherms. Journal of Petrology, 30: 1117–1158.

Fan, Q.C., Sun, Q., Li, N., and Sui, J., 2004. Periods of volcanic activity and magma evolution of the Holocene in North Hainan Island. Acta Petrologica Sinica, 20: 533–544 (in Chinese with English abstract).

Flower, M.F.J., Zhang, M., Chen, C.Y., Tu, K., and Xie, G.H., 1992. Magmatism in the South China Basin. 2 Post-spreading Quaternary basalts from Hainan Island, South China. Chemical Geology, 97: 65–87.

Frezzotti, M.L., 2001. Silicate-melt inclusions in magmatic rocks: Applications to petrology. Lithos, 55: 273–299.

Frezzotti, M.L., Tecce, F., and Casagli, A., 2012. Raman spectroscopy for fluid inclusion analysis. Journal of Geochemical Exploration, 112: 1–20.

Gazel, E., Plank, T., Forsyth, D.W., Bendersky, C., Lee, C.T.A., and Hauri, E.H., 2012. Lithosphere versus asthenosphere mantle sources at the Big Pine Volcanic Field, California. Geochemistry Geophysics Geosystems, 13: 1–25.

Harte, B. 1983. Mantle peridotites and processes. In: Hawkesworth, C.J., and Norry, M.J. (eds.), Continental Basalts and Mantle Xenoliths. Nantwich: Shiva, 4–91.

Hartley, M.E., Maclennan, J., Edmonds, M., and Thordarson, T., 2014. Reconstructing the deep CO_2 degassing behaviour of large basaltic fissure eruptions. Earth and Planetary Science Letters, 393: 120–131.

Hauri, E., 2002. SIMS analysis of volatiles in silicate glasses, 2: Isotopes and abundances in Hawaiian melt inclusions. Chemical Geology, 183: 115–141.

Hauri, E.H., Maclennan, J., McKenzie, D., Gronvold, K., Oskarsson, N., and Shimizu, N., 2017. CO_2 content beneath

northern Iceland and the variability of mantle carbon. Geology, 46: 55–58.
Hellebrand, E., Snow, J.E., Dick, H.J.B., and Hofmann, A.W., 2001. Coupled major and trace elements as indicators of the extent of melting in mid-ocean-ridge peridotites. Nature, 410: 677–681.
Ho, K.S., Chen, J.C., and Juang, W.S., 2000. Geochronology and geochemistry of late Cenozoic basalts from the Leiqiong area, southern China. Journal of Asian Earth Sciences, 18: 307–324.
Hoang, N., Flower, M.F.J., and Carlson, R.W., 1996. Major, trace element, and isotopic compositions of Vietnamese basalts: Interaction of hydrous EM1-rich asthenosphere with thinned Eurasian lithosphere. Geochimica et Cosmochimica Acta, 60: 4329–4351.
Hofmann, A.W., Jochum, K.P., Seufert, M., and White, W.M., 1986. Nb and Pb in oceanic basalts–New constraints on mantle evolution. Earth and Planetary Science Letters, 79: 33–45.
Huang, Z., Cai, F., Han, Z., Chen, J., Zong, Y., and Lin, X., 1993. Leiqiong Quaternary Volcano. Beijing: Science Press, 1–80 (in Chinese).
Hu, Z., Zhang, W., Liu, Y., Gao, S., Li, M., Zong, K., Chen, H. and Hu, S., 2015. "Wave" Signal-smoothing and mercury-removing device for Laser Ablation Quadrupole and Multiple Collector ICPMS analysis: Application to lead isotope analysis. Analytical Chemistry, 87: 1152–1157.
Ionov, D.A., Dupuy, C., Oreilly, S.Y., Kopylova, M.G., and Genshaft, Y.S., 1993. Carbonated peridotite xenoliths from Spitsbergen–Implications for trace-element signature of mantle carbonate metasomatism. Earth and Planetary Science Letters, 119: 283–297.
Ionov, D.A., Hofmann, A.W. and Shimizu, N., 1994. Metasomatism-induced melting in mantle xenoliths from Mongolia. Journal of Petrology, 35: 753–785.
Jiang, Y., Liang, X.R., Liang, X.Q., Fu, J.G., Wang, C., Zhou, Y., and Wen, S.N., 2017. Formation mechanism of East Asia continental margin extensional belt: Evidence from geochemistry study of Hainan mantle xenoliths. Geotectonica et Metallogenia, 41: 157–182 (in Chinese).
Johnson, K.T.M., Dick, H.J.B., and Shimizu, N., 1990. Melting in the oceanic upper mantle: An ion microprobe study of diopsides in abyssal peridotites. Journal of Geophysical Research, 95: 2661–2678.
Kent, A.J.R., 2008. Melt Inclusions in basaltic and related volcanic rocks. Minerals, Inclusions and Volcanic Processes, 69: 273–331.
Keppler, H., 1996. Constraints from partitioning experiments on the composition of subduction-zone fluids. Nature, 380: 237–240.
Kwak, J.H., Hu, J.Z., Turcu, R.V.F., Rosso, K.M., Ilton, E.S., Wang, C.M., Sears, J.A., Engelhard, M.H., Felmy, A.R., and Hoyt, D.W., 2011. The role of H_2O in the carbonation of forsterite in supercritical CO_2. International Journal of Greenhouse Gas Control, 5: 1081–1092.
Le Bas, M.J.L., Maitre, R.W.L., Streckeisen, A., and Zanettin, B., 1986. A chemical classification of volcanic rocks based on the Total Alkali–Silica Diagram. Journal of Petrology, 27: 745–750.
Lebedev, S., and Nolet, G., 2003. Upper mantle beneath Southeast Asia from S velocity tomography. Journal of Geophysical Research: Solid Earth, 108(B1): 2048. doi:10.1029/2000JB000073.
Lei, H.S., Zhao, Z.D., Niu, Y.L., Zhang, S.Q., Cousens, B., Ma, Q., Teng, F.Z., Liu, D., Miao, Z., Yang, Y.Y., Wu, J.K., Wang, Q., and Zhu, D.C., 2021. Identifying deep recycled carbonates through Miocene basalts in the Maguan area, SE Tibetan Plateau. Lithos, 400–401: 106356.
Lei, J., Zhao, D., Steinberger, B., Wu, B., Shen, F., and Li, Z., 2009. New seismic constraints on the upper mantle structure of the Hainan plume. Physics of the Earth and Planetary Interiors, 173: 33–50.
Li, X.H., 2021. The major driving force triggering breakup of supercontinent: Mantle plumes or deep subduction? Acta Geologica Sinica, 95(1): 20–31 (in Chinese with English abstract).
Li, X.Y., 2015. The nature and Phanerozoic evolution of the deep lithosphere under the Hunan–Guangxi region, South China (Ph.D. thesis). Wuhan: China University of Geosciences, 1–100 (in Chinese with English abstract).
Liu, J.Q., Ren, Z.Y., Nichols, A.R.L., Song, M.S., Qian, S.P., Zhang, Y., and Zhao, P.P., 2015. Petrogenesis of Late Cenozoic basalts from North Hainan Island: Constraints from melt inclusions and their host olivines. Geochimica et Cosmochimica Acta, 152: 89–121.
Liu, Y.S., Hu, Z.C., Gao, S., Gunther, D., Xu, J., Gao, C.G., and Chen, H.H., 2008. In situ analysis of major and trace elements of anhydrous minerals by LA–ICP–MS without applying an internal standard. Chemical Geology, 257: 34–43.
Loring, J.S., Chen, J., Benezeth, P., Qafoku, O., Ilton, E.S., Washton, N.M., Thompson, C.J., Martin, P.F., McGrail, B.P., Rosso, K.M., Felmy, A.R., and Schaef, H.T., 2015. Evidence for carbonate surface complexation during forsterite carbonation in wet supercritical carbon dioxide. Langmuir, 31, 27: 7533–7543.
Lowenstern, J.B., 2003 Melt inclusions come of age: Volatiles, volcanoes, and Sorby's legacy. In: De Vivo, B., and Bodnar, R.J. (eds.), Melt Inclusions in Volcanic Systems. Amsterdam: Elsevier, 1–21.
Lu, H., Lei, J., Zhao, D., Xu, Y.G., Sun, C., and Hu, X., 2022. Anisotropic tomography of Hainan Island and surrounding areas: New insights into the Hainan mantle plume. Journal of Geophysical Research: Solid Earth, 127: e2021JB023609.
Metcalfe, I., Shergold, I.H., and Li, Z.X., 1993. IGCP 321 Gondwana dispersion and Asian accretion: Fieldwork on Hainan Island. Episodes, 16: 443–447.
Mironov, N., Portnyagin, M., Botcharnikov, R., Gurenko, A., Hoernle, K., and Holtz, F., 2015. Quantification of the CO_2 budget and H_2O–CO_2 systematics in subduction-zone magmas through the experimental hydration of melt inclusions in olivine at high H_2O pressure. Earth and Planetary Science Letters, 425: 1–11.
Montelli, R., Nolet, G., Dahlen, F.A., and Masters, G., 2006. A catalogue of deep mantle plumes: New results from finite-frequency tomography. Geochemistry, Geophysics, Geosystems, 7: 1–69.
Moore, L.R., and Bodnar, R.J., 2019. A pedagogical approach to estimating the CO_2 budget of magmas. Journal of the Geological Society, 176: 398.
Moore, L.R., Gazel, E., Tuohy, R., Lloyd, A.S., Esposito, R., Steele-MacInnis, M., Hauri, E.H., Wallace, P.J., Plank, T., and Bodnar, R.J., 2015. Bubbles matter: An assessment of the contribution of vapor bubbles to melt inclusion volatile budgets. American Mineralogist, 100: 806–823.
Neumann, E.R., Wulff, P.E., Pearson, N.J., and Spencer, E.A., 2002. Mantle xenoliths from Tenerife (Canary Islands): Evidence for reactions between mantleperidotites and silicic carbonatite melts inducing Ca metasomatism. Journal of Petrology, 43: 825–857.
Nimis, P., and Ulmer, P., 1998. Clinopyroxene geobarometry of magmatic rocks Part 1: An expanded structural geobarometer for anhydrous and hydrous, basic and ultrabasic systems. Contributions to Mineralogy and Petrology, 133: 122–135.
Norman, M.D., 1998. Melting and metasomatism in the continental lithosphere: Laser Ablation ICP-MS analysis of minerals in spinel lherzolites from eastern Australia. Contributions to Mineralogy and Petrology, 130: 240–255.
O'Reilly, S.Y., and Griffin, W.L., 2010. Rates of magma ascent: Constraints from mantle-derived xenoliths. In: Dosseto, A., Turner, S.P., and Van-Orman, J.A. (eds.), Timescales of Magmatic Processes–From Core to Atmosphere. New York: John Wiley and Sons, 1–9.
Roedder, E., 1979. Origin and significance of magmatic inclusions. Bulletin de Mineralogie, 102: 487–510.
Roedder, E., 1984. Fluid inclusion. Reviews in Mineralogy, 12: 646.
Rudnick, R.L., and Gao, S., 2003. Composition of the continental crust. In: Rudnick, R.L. (ed.), Treatise of Geochemistry, Vol. 3. Amsterdam: Elsevier, 1–64.
Rudnick, R.L., McDonough, W.F., and Chappell, B.W., 1993. Carbonatite metasomatism in the northern Tanzanian mantle:

Petrographic and geochemical characteristics. Earth and Planetary Science Letters, 114: 463–475.

Schaef, H.T., McGrail, B.P., Loring, J.L., Bowden, M.E., Arey, B.W., and Rosso, K.M., 2013. Forsterite (Mg_2SiO_4) carbonation in wet supercritical CO_2: An in situ high-Pressure X-ray diffraction study. Environmental Science & Technology, 47: 174–181.

Schiano, P., and Clocchiatti, R., 1994. Worldwide occurrence of silica rich melts in sub-continental and sub-oceanic mantle minerals. Nature, 368: 621–624.

Schiano, P., and Clocchiatti, R., 1992. Melt and fluid inclusions in basalts and xenoliths from Tahaa Island, Society archipelago evidence for a metasomatized upper mantle. Earth and Planetary Science Letters, 111: 69–82.

Shaw, A.M., Behn, M.D., Humphris, S.E., Sohn, R.A., and Gregg, P.M., 2010. Deep pooling of low degree melts and volatile fluxes at the 85°E segment of the Gakkel Ridge: Evidence from olivine-hosted melt inclusions and glasses. Earth and Planetary Science Letters, 289: 311–322.

Shaw, A.M., Hauri, E.H., Fischer, T.P., Hilton, D.R., and Kelley, K.A., 2008. Hydrogen isotopes in Mariana arc melt inclusions: Implications for subduction dehydration and the deep-earth water cycle. Earth and Planetary Science Letters, 275: 138–145.

Sleep, N.H., and Zahnle, K., 2001. Carbon dioxide cycling and implications for climate on ancient Earth. Journal of Geophysical Research: Planets, 106: 1373–1399.

Stopic, S., Dertmann, C., Modolo, G., Kegler, P., Neumeier, S., Kremer, D., Wotruba, H., Etzold, S., Telle, R., Rosani, D., Knops, P., and Friedrich, B., 2018. Synthesis of magnesium carbonate via carbonation under high pressure in an autoclave. Metals, 8: 993.

Sun, P., Niu, Y.L., Guo, P.Y., Chen, S., Duan, M., Gong, H.M., Wang, X.H., and Xiao, Y.Y., 2018. Multiple mantle metasomatism beneath the Leizhou Peninsula, South China: Evidence from elemental and Sr-Nd-Pb-Hf isotope geochemistry of the late Cenozoic volcanic rocks. International Geology Review, 61: 1768–1785.

Sun, Q., 2003. Quaternary volcanic activity and magma evolution in north Hainan Island (Ph.D. thesis). Beijing: Institute of Geology, Chinese Seismological Bureau, 1–78 (in Chinese with English abstract).

Sun, S.S., and McDonough, W.F., 1989. Chemical and isotopic systematics of oceanic basalts: implications for mantle composition and processes. Geological Society, London, Special Publications, 42: 313–345.

Sun, Z., Zhong, Z., Keep, M., Zhou, D., Cai, D., Li, X., Wu, S., and Jiang, J., 2009. 3D analogue modeling of the South China Sea: A discussion on breakup pattern. Journal of Asian Earth Sciences, 34: 544–556.

Tang, H.F., Guo, T.C., Wu, K.Q., Liu, Z.L., Xu, J.Y., Lu, B.L., and Wang, P.J., 2022. Reassessment of the Distribution of Mantle CO_2 in the Bohai Sea, China: The Perspective from the Source and Pathway System. Acta Geologica Sinica (English edition), 96(1): 337–347.

Taylor, S.R., 1964. Abundance of chemical elements in the continental crust: A new table. Geochimica et Cosmochimica Acta, 28: 1273–1285.

Tucker, J.M., Hauri, E.H., Pietruszka, A.J., Garcia, M.O., Marske, J.P., and Trusdell, F.A., 2019. A high carbon content of the Hawaiian mantle from olivine-hosted melt inclusions. Geochimica et Cosmochimica Acta, 254: 156–172.

Tuohy, R.M., Wallace, P.J., Loewen, M.W., Swanson, D.A., and Kent, A.J.R., 2016. Magma transport and olivine crystallization depths in Kīlauea's east rift zone inferred from experimentally rehomogenized melt inclusions. Geochimica et Cosmochimica Acta, 185: 232–250.

Wallace, P.J., 2005. Volatiles in subduction zone magmas: Concentrations and fluxes based on melt inclusion and volcanic gas data. Journal of Volcanology and Geothermal Research, 140: 217–240.

Wallace, P.J., Kamenetsky, V.S., and Cervantes, P., 2015. Melt inclusion CO_2 contents, pressures of olivine crystallization, and the problem of shrinkage bubbles. American Mineralogist, 100: 787–794.

Wan, Z., Coogan, L.A., and Canil, D., 2008. Experimental calibration of aluminum partitioning between olivine and spinel as a geothermometer. American Mineralogist, 93: 1142 –1147.

Wang C., Jin, Z.M., Gao S., 2010. Eclogite-melt/peridotite reaction: Experimental constrains on the destruction mechanism of the North China Craton. Science China Earth Sciences, 40: 541–555.

Wang, S., Kuang, J., Huang, X.L., Zhang, H.Y., Zhang, M., Qi., S.H., Han, Y.J., Xiao, Z.C., Wang, S.Q., and Tang. L., 2022. Upwelling of mantle-derived material in Southeast China: Evidence from Noble Gas isotopes. Acta Geologica Sinica (English Edition), 96(1): 100–110.

Wang, P.Y., Gu, X.Y., Kuritani, T., Hanski, E., and Xia, Q.K., 2021. Highly variable H_2O/Ce ratios in the Hainan mantle plume. Lithos, 406–407: 106516.

Wang, X.C., Li, Z.X., Li, X.H., Li, J., Liu, Y., Long, W.G., Zhou, J.B., and Wang, F., 2012. Temperature, pressure, and composition of the mantle source region of late Cenozoic basalts in Hainan Island, SE Asia: A consequence of a young thermal mantle plume close to subduction zones? Journal of Petrology, 53: 177–233.

Wang, X.C., Li, Z.X., Li, X.H., Li, J., Xu, Y.G., and Li, X.H., 2013. Identification of an ancient mantle reservoir and young recycled materials in the source region of a young mantle plume: Implications for potential linkages between plume and plate tectonics. Earth and Planetary Science Letters, 377–378: 248–259.

Wanless, V.D., Behn, M.D., Shaw, A.M., and Plank, T., 2014. Variations in melting dynamics and mantle compositions along the Eastern Volcanic Zone of the Gakkel Ridge: Insights from olivine–hosted melt inclusions. Contributions to Mineralogy and Petrology, 167: 1005.

Wanless, V.D., Shaw, A.M., Behn, M.D., Soule, S.A., Escartín, J., and Hamelin, C., 2015. Magmatic plumbing at Lucky Strike volcano based on olivine-hosted melt inclusion compositions. Geochemistry, Geophysics, Geosystems, 16: 126–147.

Wei, F.X., Wei, W., and Yu, H.M., 2021. The Cenozoic volcanic fields in northern Hainan Island and the Leizhou Peninsula, south China: Eruption history, magma source and dynamic background. Geological Society, London, Special Publications, 510: 179.

Wells, P.R.A., 1977. Pyroxene thermometry in simple and complex systems. Contributions to Mineralogy and Petrology. 62: 129–139.

Wieser, P.E., Lamadrid, H., Maclennan, J., Edmonds, M., Matthews, S., Iacovino, K., Jenner, F.E., Gansecki, C., Trusdell, F., Lee, R.L., and Ilyinskaya, E., 2020. Reconstructing magma storage depths for the 2018 Kilauean eruption from melt inclusion CO_2 contents: The importance of vapor bubbles. Geochemistry, Geophysics, Geosystems, 22: e2020GC009364.

Wood, B.J., and Banno, S., 1973. Garnet–orthopyroxene and orthopyroxene–clinopyroxene relationships in simple and complex systems. Contributions to Mineralogy and Petrology, 42: 109–124.

Wu, H.H., Tsai, Y.B., Lee, T.Y., Lo, C.H., Hsieh, C.H., and Toan, D.V., 2005. 3-D shear wave velocity structure of the crust and upper mantle in the South China Sea and its surrounding regions by surface wave dispersion analysis. Marine Geophysical Researches, 25: 5–27.

Xia, S.H., Zhao, D.P., Sun, J.L., and Huang, H.B., 2016. Teleseismic imaging of the mantle beneath southernmost China: New insights into the Hainan plume. Gondwana Research, 36: 46–56.

Xu, Y., Yang, Y.M., Yu, H.J., Gao, W., Gao, X.X., Liu, B.H., Tian, X., Yang, J.C., and Zhang, W.Q., 2020. Geochemistry and petrogenesis of volcanic rocks from the continent–ocean transition zone in the northern South China Sea and their tectonic implications. Journal of the Ocean University of China, 19: 1051–1061.

Xu, Y.G., Sun, M., Yan, W., Liu, Y., Huang, X.L., and Chen, X.M., 2002. Xenolith evidence for polybaric melting and stratification of the upper mantle beneath South China.

Journal of Asian Earth Sciences, 20: 937–954.
Yan, Q.S., Shi, X.F., Metcalfe, I., Liu, S.F., Xu, T.Y., Kornkanitnan, N., Sirichaiseth, T., Yuan, L., Zhang, Y., and Zhang, H., 2018. Hainan mantle plume produced late Cenozoic basaltic rocks in Thailand, Southeast Asia. Scientific Reports, 8: 2640.
Yaxley, G.M., and Green, D.H., 1998. Reactions between eclogite and peridotite: Mantle refertilisation by subduction of oceanic crust. Schweizerische Mineralogische Und Petrographische Mitteilungen, 78: 243–255.
Zhao, D.P., 2007. Seismic images under 60 hotspots: Search for mantle plumes. Gondwana Research, 12: 335–355.
Zhao, D.P., Toyokuni, G., and Kurata, K., 2021. Deep mantle structure and origin of Cenozoic intraplate volcanoes in Indochina, Hainan and South China Sea. Geophysical Journal International, 225: 572–588.
Zimbelman, J.R., and Gregg, T.K.P., 2000. Environmental effects on volcanic eruptions: From deep oceans to deep space. New York: Kluwer Academic/Plenum Publishers, 1–260.
Zong, K.Q., and Liu, Y.S., 2018. Carbonate metasomatism in the lithospheric mantle: Implications for cratonic destruction in North China. Science China Earth Sciences, 61: 711–729 (in Chineses with English abstract).
Zou, H.B., and Fan, Q.C., 2010. U-Th isotopes in Hainan basalts: Implications for sub-asthenospheric origin of EM2 mantle endmember and the dynamics of melting beneath Hainan Island. Lithos, 116: 145–152.

About the first author

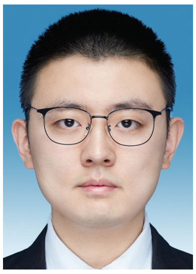

XU Xin, male, born in 1992 in Yulin, Shannxi Province; master; graduated from China’s University of Geosciences, Beijing; Ph.D. student of the School of Earth and Space Sciences, Peking University. He is currently interested in igneous geology. E-mail: xuxin@stu.pku.edu.cn.

About the corresponding author

ZHANG Lifei, born in 1963 in Siping City, Jilin Province; Ph.D.; graduated from Peking University; professor of the School of Earth and Space Sciences, Peking University. He is currently interested in metamorphic geology. E-mail: lfzhang@pku.edu.cn.